JGR Solid Earth

RESEARCH ARTICLE
10.1029/2020JB021321

Mechanical Compaction of Crustal Analogs Made of Sintered Glass Beads: The Influence of Porosity and Grain Size

Lucille Carbillet[1], Michael J. Heap[1], Patrick Baud[1], Fabian B. Wadsworth[2], and Thierry Reuschlé[1]

[1]Institut Terre et Environnement de Strasbourg, Université de Strasbourg, CNRS UMR 7063, Strasbourg, France, [2]Department of Earth Sciences, Science Labs, Durham University, Durham, UK

Abstract The fundamentals of our understanding of the mechanical compaction of porous rocks stem from experimental studies. Yet, many of these studies use natural materials for which microstructural parameters are intrinsically coupled, hampering the diagnosis of relationships between microstructure and bulk sample behavior. To probe the influence of porosity and grain size on the mechanical compaction of granular rocks, we performed experiments on synthetic samples prepared by sintering monodisperse populations of glass beads, which allowed us to independently control porosity and grain diameter. We conducted hydrostatic and triaxial compression tests on synthetic samples with grain diameters and porosities in the ranges 0.2–1.15 mm and 0.18–0.38 mm, respectively. During hydrostatic compaction, sample porosity decreased suddenly and substantially at the onset of inelastic compaction due to contemporaneous and extensive grain crushing, a consequence of the monodisperse grain size. During triaxial tests at high confining pressure, our synthetic samples failed by shear-enhanced compaction and showed evidence for the development of compaction bands. Critical stresses at the onset of inelastic compaction map out linear-shaped yield caps for the porosity-grain diameter combinations for which the critical stress for inelastic hydrostatic compaction is known. Our yield caps reinforce the first-order importance of porosity on the compactive yield strength and show, all else being equal, that grain size also exerts a first-order control and should therefore be routinely measured. Our study further reveals the suitability of sintered glass beads as analogs for crustal rocks, which facilitate the study of the deconvolved influence of microstructural parameters on their mechanical behavior.

Plain Language Summary Porous rocks that form the shallow part of the Earth's crust are submitted to pressure conditions under which they deform by compaction, that is, their porosity is reduced. Our understanding of the compaction stems primarily from laboratory experiments conducted on samples of natural rocks. Yet, because the internal structure of natural materials is complex, studying the influence of structural parameters in isolation, such as porosity and grain size, on the way rock compacts is limited. To tackle this issue, we conducted compression tests on synthetic samples made of fused glass beads for which we could control porosity and grain size. When the pressure on the synthetic rocks is increased uniformly in all directions, a threshold pressure, characteristic of the rock strength, is reached beyond which they compact suddenly and substantially. When a differential stress is imposed on the synthetic rocks, discrete bands of lower porosity are observed. We show that porosity and grain size exert a first-order control on the ability of the synthetic rocks to resist compaction. Further, our synthetic samples are good analogs for natural rocks such as sandstones and tuffs and our results therefore have broad applications, from reservoir compaction and subsidence to the destabilization of volcanoes.

Key Points:

- The mechanical compaction behavior of monodisperse sintered glass bead samples is similar to that of well-sorted monomineralic sandstones
- During triaxial compression at high confining pressure, discrete compaction bands developed in a synthetic sample with a porosity of 0.35
- All else being equal, increasing grain diameter from 0.2 to 1.15 mm decreases the stress to reach C^* by more than a factor of two

Correspondence to:
L. Carbillet,
lcarbillet@unistra.fr

Citation:
Carbillet, L., Heap, M. J., Baud, P., Wadsworth, F. B., & Reuschlé, T. (2021). Mechanical compaction of crustal analogs made of sintered glass beads: The influence of porosity and grain size. *Journal of Geophysical Research: Solid Earth*, *126*, e2020JB021321. https://doi.org/10.1029/2020JB021321

Received 9 NOV 2020
Accepted 15 MAR 2021

1. Introduction

The mechanical compaction of porous materials is an important process in the Earth's crust. It is one of the main deformation mechanisms of lithification, diagenesis, fault growth, and/or sealing, and plays a key role in many processes in sedimentary settings such as reservoirs, aquifers, and basins (Bjørlykke, 2006; Guéguen & Boutéca, 2004; Taylor et al., 2008), and in volcanic settings (Grunder & Russell, 2005; Farquharson et al., 2017; Quane et al., 2009). Understanding the phenomenology and micromechanics of compaction rests upon the ability to characterize the evolution of microstructure through compactant deformation.

To predict the occurrence and extent of mechanical compaction, knowledge of the relationship between rock microstructural attributes and bulk mechanical properties is crucial. Indeed, the effective macroscopic properties of heterogeneous materials such as crustal rocks intricately depend on the phases present, their volume fraction, their spatial distribution, and their properties (e.g., Torquato, 2002). Therefore, relating microstructural attributes of porous rock to bulk properties has been the focus of numerous studies in the past decades, the majority of which relied on direct experimental measurements or numerical simulations (Blair et al., 1993; Doyen, 1988; Eberhart-Phillips et al., 1989; Ghazvinian et al., 2014; Schöpfer et al., 2009; Scott & Nielsen, 1991).

As early as 1990, it had already been suggested the two principle microstructural controls on the mechanical and hydraulic properties of sedimentary rocks were (1) porosity and (2) grain size (Bourbie & Zinszner, 1985; Paterson & Wong, 2005; Rutter & Glover, 2012; Zhang et al., 1990). Broadly speaking, an increase in rock porosity causes a decrease in strength (e.g., Baud et al., 2014; Chang et al., 2006) and an increase in permeability (Bernabé et al., 2003; Dardis & Mccloskey, 1998). In detail, porosity also exerts an influence on the type of failure that can result from the application of crustal stresses (i.e., brittle or ductile). Low-porosity rock will remain brittle even under a wide range of pressure conditions (analogous to depth), whereas high-porosity rock will only behave in a brittle manner at relatively low pressure and will transition to ductile behavior at high-pressure (Wong & Baud, 2012; Wong et al., 1997). Alongside the influence exerted by porosity, grain size has also been the target of an increasing number of experimental studies which demonstrated its controlling influence on mechanical and hydraulic properties (Atapour & Mortazavi, 2018; Schultz et al., 2010; Wasantha et al., 2015). However, when considering porosity and grain size, one usually refers to average values for the bulk volume of samples. As pores and grains are not always homogeneously distributed, a more accurate way to describe microstructure is to use pore and grain size distributions. Grain size distribution in lithified sedimentary rocks is also known to influence the mechanical behavior and failure mode (Guéguen & Fortin, 2013; Weng & Li, 2012; Xu et al., 2020), notably the possible development of compaction localization at high effective pressures (Baud et al., 2004). Assuming that grain crushing initiates by Hertzian fracture at grain contacts, Zhang et al. (1990) proposed a micromechanical model predicting the stress required to achieve grain crushing using porosity and grain size. While the model by Zhang et al. (1990) is in basic agreement with the existing data set, Rutter and Glover (2012) suggested that data for sandstones would be better described by a different empirical law. Moreover, the scatter on compiled experimental data remains large (Baud et al., 2014; Chang et al., 2006). Indeed, trends in plots of strength as a function of porosity or grain size are complicated by the fact that other microstructural parameters, such as pore size and shape, their distributions, or matrix composition, change together with porosity and grain size. For example, a decrease in porosity is often associated with an increase in the proportion of cement, that, if located along grain boundaries, can greatly increase the strength of granular materials (Baud et al., 2017; David et al., 1998; de Bono et al., 2015; Haeri et al., 2005; Yin & Dvorkin, 1994). These complexities arise from the fact that the influence of porosity, grain size, and these other microstructural considerations are all interconnected and that ultimately a fruitful way forward would be to find a method by which they can be deconvolved and studied in isolation.

The uncertainty ensuing from the strong coupling between microstructural parameters, the inherent variability from sample to sample and the heterogeneity of natural materials limits the extent to which experimental studies can draw definitive conclusions about the influence of specific microstructural attributes on the mechanical properties of natural materials. To tackle this issue, several strategies could be considered: experiments using particularly simple materials occurring with a broad range of porosity such as Fontainebleau sandstone (Saadi et al., 2017; Sulem & Ouffroukh, 2006) or Leitha limestone (Baud et al., 2017); simulations using numerical samples (Schöpfer et al., 2009; Weng & Li, 2012); or experiments using synthetic samples (Bouzidi & Schmitt, 2012; Castagna & Backus, 1993; Chapman et al., 2018; David et al., 1998; Plona et al., 1980). In this study, we chose to follow the rationale of Berge et al. (1995), Guyon et al. (1987), and Wadsworth et al. (2016) who proposed sintered soda-lime silica glass beads as suitable analogs for granular crustal rocks, such as sandstones and tuffs. Silicate glass compositions have been extensively studied and data pertaining to their properties have been gathered in handbooks for various applications (e.g., Bansal & Doremus, 2013). The elastic properties of soda-lime silica glass are comparable to those of granular sedimentary and volcanic rocks (Berge et al., 1995; Vasseur et al., 2016). Additionally, in nature, grains that go through the different steps of diagenesis and form variably porous upper crust material are well

Table 1
Chemical Composition of Glass Beads (Provided by Manufacturer) Used in This Study

Oxide	SiLiBeads (wt %)	SpheriGlass (A-Glass) (wt %)
SiO_2	72.95	72.5
Na_2O	13.08	13.7
CaO	9.06	9.8
MgO	4.25	3.3
Al_2O_3	0.58	0.4
FeO/Fe_2O_3	–	0.2
K_2O	–	0.1

N.b. All wt % are recalculated to 100% disregarding the minor effect of loss on ignition.

approximated, to a first-order, by sintering beads. Viscous sintering of glass beads then allows for the reproduction of the granular to nongranular transition and the preparation of synthetic rocks of predetermined final porosity and grain size (Wadsworth et al., 2016).

In this paper, we present results of a suite of mechanical tests performed on synthetic samples made of monodisperse distributions of glass beads. After describing the preparation technique and the intact microstructure of our synthetic samples, we present the mechanical data and the associated failure mode. These results are discussed, and we will focus on the following questions. Mechanically speaking, how do the sintered glass beads samples compare with natural sandstones? Quantitatively, what is the influence of grain size and porosity on mechanical compaction? Considering the importance of compaction bands in the fields of rock mechanics, hydrology, and geology, could this failure mode be reproduced in synthetic samples?

2. Preparation and Characterization of the Synthetic Samples

2.1. Viscous Sintering of Monodisperse Populations of Glass Beads

When heated above the glass transition temperature interval, glass beads become viscous droplets. If these glass beads are packed together when heated then, as they transition from glass beads to viscous droplets, they can interact and coalesce in a process referred to as viscous sintering (Frenkel, 1945; Mackenzie & Shuttleworth, 1949; Wadsworth et al., 2016). The dominant consequence of viscous sintering is that the porosity is reduced with time. Because it is temperature-activated, this process has advantages for producing idealized porous materials. A desired packing arrangement, or grain size distribution can be determined in the cold, room temperature state, and then via heating, viscous sintering processes can be used to evolve that state to lower porosities.

Viscous sintering is driven by interfacial tension between the glass beads and the interstitial gas between the beads (Kuczynski, 1949). During viscous sintering, an initial system of viscous droplets evolves with time through two main stages: (1) the growth of necks between droplet-droplet pairs that share a contact (Frenkel, 1945), and (2) the shrinkage and closure of the pores between the droplets (Mackenzie & Shuttleworth, 1949). The initial system of viscous spherical droplets and interstitial pores evolves into a system of isolated pores within a viscous liquid continuum. That is, the end-state (gas in a liquid) is the inverse of the starting state (liquid in a gas) (Wadsworth et al., 2017). In practice, in order to reach a desired porosity in a desired time for a given grain size of glass bead, we control the temperature of synthesis (Wadsworth et al., 2016). The effect of changing the grain size is to change the pore size between the grains; therefore, the ability to tweak the grain size of the starting glass bead population allows us to control the pore size distribution independently from the porosity, effectively deconvolving these structural controls.

We prepared three sets of samples using monodisperse populations of glass spheres of diameter between 0.15 and 0.25 mm (Spheriglass A-Glass 1922 from Potters Industries Inc.), 0.4 and 0.6 mm (SiLibeads Glass beads type S 5218-7), or 1 and 1.3 mm (SiLibeads Glass beads type S 4504) of similar chemical composition (Table 1). The corresponding grain diameter distributions are presented in Figure 1a. The synthetic rocks were prepared as blocks from which samples were cored. For each block, a monodisperse distribution of beads was poured into a ceramic tray of dimensions 205 × 125 × 50 mm. The tray was then manually shaken to flatten out the beak pack surface and then placed inside an electric box furnace (L9/11/SKM by Nabertherm). The box furnace was set to heat at a constant rate of 3°C min^{-1} to 680°C, which is above the glass transition onset temperature of 549°C provided by the manufacturer (similar for both bead type; Table 1). The peak sintering temperature was maintained constant for 1–12 h depending on the target final porosity (longer times result in lower porosity). The tray was moved to 180° of its initial position halfway through the dwell to reduce the heterogeneity of the sintered block that may arise when the temperature distribution in a furnace is not even. After being held constant for a fixed time, the temperature in the furnace was lowered to 500°C at a cooling rate of 1°C min^{-1} and finally decreased to ambient temperature

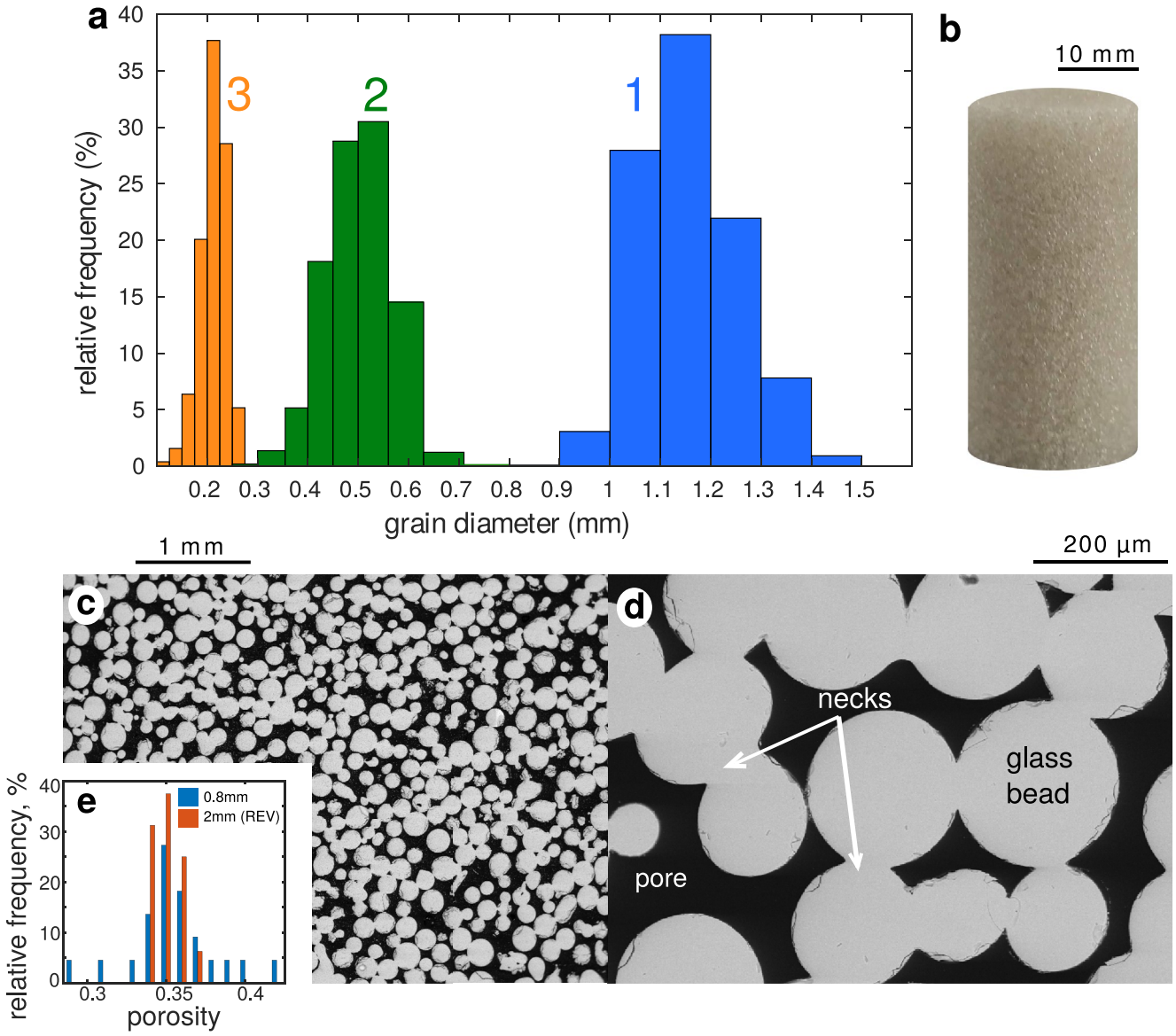

Figure 1. Microstructural description of the synthetic samples. (a) Grain diameter distributions corresponding to the different mean grain diameter considered, 3: 0.15–0.25 mm (orange), 2: 0.4–0.6 mm (green), 1: 1.0–1.3 mm (blue). Although these distributions are not technically monodisperse but monomodal, we herein use the term monodisperse to describe our samples. (b) Photograph of a synthetic sample with a porosity of 0.35 and a mean grain diameter of 0.2 mm and (c) corresponding scanning electron micrograph of its microstructure (black: porosity, gray: glass). (d) Scanning electron micrograph showing the necks that have grown between initially adjacent beads during sintering. (e) 2D porosity distributions measured for the same sample using a window with a 0.8 mm edge-length (blue) or with a 2 mm edge-length (representative elementary volume, red) using image processing program ImageJ. Frequencies cluster around 0.35, which corresponds to the porosity measured in laboratory.

at a cooling rate of 3°C min^{-1}. This cooling workflow was designed to minimize thermal microcracking. Cylindrical samples of 20 mm diameter were cored along the horizontal axis of the resulting sintered block to minimize gravity induced porosity gradients along the axis of the samples. These samples were then cut and precision-ground to a nominal length of 40 mm.

2.2. Description of the Sintered Glass Beads Samples

A photograph of one of the synthetic samples is provided as Figure 1b. Insights into the microstructure of the synthetic samples were gained using polished thin sections observed under a scanning electron

microscope (SEM) (Figures 1c and 1d). The SEM images were acquired on a polished slice of a sample with a porosity of 0.35 and a mean grain diameter of 0.2 mm. As predicted by the Frenkel model, adjacent beads are connected by a neck and pore space remains between the bonded grains (Figure 1d). The lowest porosity obtained in this study is 0.22. Therefore, all our samples are in the range between high porosity, close to the initial packing porosity where incipient sintering has only formed necks, and intermediate porosity, where sintering has progressed and begun to close the pore network. Our study does not encompass low-porosity synthetic rocks which would exhibit pore structures close to isolated pores in a glass medium (the equilibrium porosity at the end of sintering is 0.03; Wadsworth et al., 2016). Thus, all our samples are in the upper range of porosity encompassed by natural granular rocks. While a material is only truly granular when the individual grains can move relative to one another (which is the case for the glass beads prior to sintering), our synthetic rocks are close to that granular end member case. The microstructure of an assembly of soda-lime silica glass spheres that underwent densification by sintering to a more advanced stage have been imaged in 2D by Vasseur et al. (2016) and continuously in 3D by Wadsworth et al. (2017), who performed X-ray computed-tomography. These studies showed that the topological inversion of the viscous system takes place continuously through sintering, hence allowing for the construction of a unified physical description for the evolution of porosity and permeability during viscous sintering.

Although statistically homogeneous, the granular materials prepared here by sintering glass spheres present heterogeneities on the scale of 2–3 grains. Indeed, SEM images of intact samples reveal small heterogeneities in the pore size distribution (Figure 1c). As our preparation workflow allows for controlling the diameter of the grains and the degree of polydispersivity but not for designing the exact nature and structure of the porous space, some porous patches, whose width can reach 0.4 mm, can be observed in our intact samples (Figure 1c). Using square windows of 0.8 mm of edge-length and of 2 mm of edge-length, 2D porosity measurements were performed on SEM images of intact samples (using ImageJ). The square window with an edge-length of 2 mm ensures that the measured area contains at least 10 glass beads in any one direction, to ensure a representative element volume (REV), and the square window with an edge-length of 0.8 mm allows us to better understand whether there are variations in porosity on a smaller scale. Figure 1e presents histograms of the distributions of 2D porosity measurements obtained for the zoomed-out SEM image in Figure 1c. While porosity measurements performed in the larger window provide a monomodal distribution closely clustered around 0.35, porosity measurements performed in the smaller window yield local values up to 0.42 in a sample with an average porosity of 0.35. We refer to these volumes as porosity clusters. In addition, the absence of cement is accompanied by heterogeneities in the local grain contacts geometry, as previously reported by den Brok et al. (1997). Sintered porous materials are random heterogeneous but isotropic porous media in terms of their microstructure, where we use "heterogeneous" to refer to the lack of structural order. However, our samples are homogeneous in the sense that the random variation in the microstructure occurs on length scales much less than the sample lengths.

3. Experimental Procedures

To study mechanical compaction using synthetic samples, we conducted a suite of mechanical tests on sintered glass bead samples. We performed hydrostatic and conventional triaxial compression experiments. During hydrostatic experiments the principal stresses are equal in all directions, that is, the state of stress is $\sigma_1 = \sigma_2 = \sigma_3$. During triaxial experiments, an axial stress is superimposed onto a hydrostatic pressure. The principal stress parallel to the axis of the sample is higher than the principal stresses normal to this axis, that is, the state of stress is $\sigma_1 > \sigma_2 = \sigma_3$. Although we focus here on compaction, we performed a few triaxial tests at relatively low pressure to identify the brittle-ductile transition. A summary of all our experiments is provided in Table 2. The solid density of glass beads was determined using a helium pycnometer (Micromeritics AccuPyc II 1340) prior to and after sintering at 680°C. We found that the solid density of the glass beads, 2.49 g/cm^3, was unchanged following exposure to 680°C. As we know the solid density of the glass beads, porosity was derived from the dimensions and the mass of the samples. The mean error associated with the porosity measurement is 0.005 (Table 2). The permeability of the samples was measured prior to deformation using a benchtop gaz (nitrogen) permeameter. Permeability was measured under a confining pressure of 1 MPa using the steady-state method (following the method detailed in Heap et al., 2017). All experiments were conducted at the Ecole et Observatoire des Sciences de la Terre (EOST) in Strasbourg (France)

Table 2
Experimental Conditions and Mechanical Data of the Synthetic Samples Tested in This Study

Sample	Porosity	± (mean error = 0.005)	Confining pressure P_c (MPa)	Pore pressure P_p (MPa)	Effective pressure $P_{eff} = P_c - P_p$ (MPa)	Peak stress σ_v		Yield stress C^*	
						P (MPa)	Q (MPa)	P (MPa)	Q (MPa)
Mean Grain Diameter 1.15 mm									
1814	0.181	0.004	–	–	0	10	30	–	–
1812	0.183	0.003	40	10	30	–	–	92	185
1816	0.189	0.004	60	10	50	–	–	115	194
1412	0.271	0.005	30	10	20	38	55	–	–
1414	0.265	0.005	70	10	60	–	–	80	59
1419	0.262	0.005	100	10	90	–	–	105	45
1413	0.269	0.005	130	10	120	–	–	132	35
1411	0.271	0.005	160	10	150	–	–	159	28
114012	0.294	0.006	–	–	0	1.4	4.3	–	–
114013	0.302	0.006	40	10	30	36	17	–	–
114011	0.308	0.006	70	10	60	74	43	–	–
1314	0.294	0.006	100	10	90	–	–	102	35
1313	0.303	0.006	130	10	120	–	–	128	23
114016	0.294	0.006	–	10	Hydrostatic	–	–		*P**
								156	0
Mean Grain Diameter 0.5 mm									
2317	0.255	0.005	–	–	0	10	31	–	–
23111	0.249	0.005	40	10	30	74	132	–	–
2316	0.256	0.005	70	10	60	–	–	92	97
2318	0.258	0.005	110	10	100	–	–	133	100
2313	0.263	0.005	160	10	150	–	–	177	80
2314	0.256	0.005	190	10	180	–	–	200	60
22114	0.299	0.006	–	–	0	20	7	-	-
2218	0.302	0.006	30	10	20	–	–	40	59
27312	0.304	0.006	50	10	40	–	–	61	63
22111	0.292	0.006	70	10	60	–	–	83	70
27314	0.295	0.006	90	10	80	–	–	99	58
27315	0.294	0.006	110	10	100	–	–	117	52
22213	0.301	0.006	120	10	110	–	–	125	45
27313	0.299	0.006	130	10	120	–	–	133	39
2213	0.299	0.006	150	10	140	–	–	152	36
2217	0.296	0.006	170	10	160	–	–	168	23
27311	0.295	0.006	–	10	Hydrostatic	–	–		*P**
								173	0
Mean Grain Diameter 0.2 mm									
31012	0.225	0.005	–	–	0	20	59	–	–
31,13	0.220	0.004	40	10	30	–	–	87	172
31013	0.222	0.004	70	10	60	–	–	130	212
37	0.226	0.005	90	10	80	–	–	150	212
31113	0.256	0.005	70	10	60	–	–	109	147

Table 2
Continued

Sample	Porosity	± (mean error = 0.005)	Confining pressure P_c (MPa)	Pore pressure P_p (MPa)	Effective pressure $P_{eff} = P_c - P_p$ (MPa)	Peak stress σ_v		Yield stress C^*	
						P (MPa)	Q (MPa)	P (MPa)	Q (MPa)
31110	0.266	0.006	130	10	120	–	–	177	170
311	0.262	0.005	160	10	150	–	–	200	150
31114	0.255	0.005	190	10	180	–	–	225	135
3813	0.300	0.005	40	10	30	68	115	–	–
3814	0.307	0.006	70	10	60	–	–	92	95
3413	0.305	0.006	130	10	120	–	–	146	77
3411	0.299	0.006	190	10	180	–	–	200	61
3311	0.346	0,007	30	10	20	–	–	35	46
3612	0.353	0.008	50	10	40	–	–	58	55
339	0.351	0.008	70	10	60	–	–	74	42
3314	0.356	0.007	90	10	80	–	–	91	33
3312	0.357	0.008	–	10	Hydrostatic	–	–	P^*	
								118	0
3710	0.385	0.009	40	10	30	–	–	37	22
379	0.387	0.009	50	10	40	–	–	46	19
3711	0.385	0.007	60	10	50	–	–	54	13
3712	0.382	0.007	–	10	Hydrostatic	–	–	P^*	
								69	0

Triaxial tests were conducted at nominal strain rates of 10^{-5} s^{-1}.

following the procedure detailed by Baud et al. (2015). All samples underwent the same preparation before the experiments. First, the samples were encased in very thin (<1 mm thick) copper foil jackets to preserve bulk sample cohesion following deformation (so that thin sections could be prepared) and to avoid disking. The samples were then dried in a vacuum oven at 40°C for at least 48 h and then vacuum-saturated with deionized water. Before each test, the sample to be deformed was positioned between two steel end-caps, the bottom one of which has a concentric hole at the center for fluid access to the pore pressure system. In addition, the bottom end-cap was separated from the sample by a thin highly permeable filter, made from coffee filter paper, to prevent broken beads from infiltrating the pore pressure piping during the experiments. Viton® tubing was used to separate the sample from the confining pressure system. All experiments were performed at room temperature on water-saturated samples. Computer-controlled stepping motors were used to independently regulate the confining pressure, pore fluid pressure and axial stress. Data were acquired with a sampling period of 10 s for hydrostatic experiments and 1 s for triaxial compression experiments.

For both hydrostatic and triaxial compression tests, the confining pressure P_c (kerosene) and the pore fluid pressure P_p (deionized water) were first slowly increased to their target values using servocontrolled pumps (see Table 2 for values). A fixed pore fluid pressure P_p of 10 MPa was used for all experiments and we assume a simple effective pressure law $P_{eff} = P_c - P_p$, operative for rock failure under static conditions, as shown for sandstones by Baud et al. (2015) in the brittle and ductile regimes. For the hydrostatic tests, the effective pressure P_{eff} was increased in small steps from its initial value of 2 MPa until the critical stress state for the onset of grain crushing P^* (Zhang et al., 1990), or the upper pressure limit of the press ($P_c = 200$ MPa), was reached. We waited for microstructural equilibrium at each step before increasing the confining pressure further. To do this, we assume that microstructural equilibrium was achieved when the rate of the pore volume change (recorded by monitoring the displacement of the piston in the pore pressure intensifier) was lower than 10^{-2} s^{-1}. The amount by which P_{eff} was increased at each step varied from 1 to 10 MPa depending on the time necessary to reach microstructural equilibrium at the previous step. For triaxial experiments,

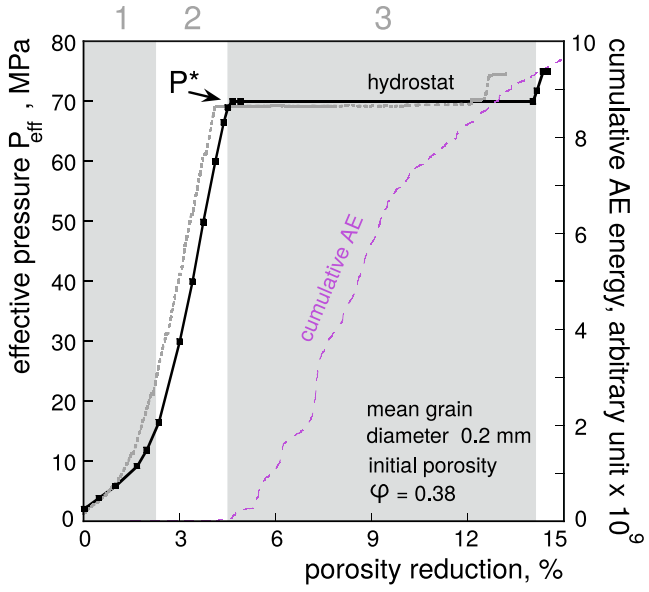

Figure 2. Representative mechanical data (black line) and cumulative acoustic emission energy (purple dashed line) for hydrostatic tests performed on the synthetic samples. These data were obtained on synthetic samples of mean grain diameter of 0.2 mm and initial porosity of 0.38. The critical stress for the onset of grain crushing P^* is indicated by an arrow. The porosity reduction in percentage corresponds to the absolute loss of porosity, that is, a porosity reduction of 14% refers to a drop from 0.38 to 0.24. (1) When P_{eff} is first increased, porosity decreases nonlinearly as a result of grains rearrangements. (2) As P_{eff} is increased further, the sample undergoes elastic deformation until P_{eff} reaches the critical value P^* beyond which (3) the sample porosity decreases suddenly and significantly by grain crushing (inelastic deformation).

once the targeted effective pressure P_{eff} was reached (i.e., hydrostatic pressurization, see Table 2 for values), the system was left to equilibrate until the pore fluid change was lower than 10^{-2} s^{-1}. Then, at constant P_{eff}, the sample was loaded as the upper piston was lowered at a fixed servocontrolled rate corresponding to a nominal strain rate of 10^{-5} s^{-1}. Considering the range of permeabilities of the synthetics (from 10^{-13} to 10^{-11} m^2, measured at a P_c of 1 MPa), the strain rate applied during triaxial compression was low enough to ensure drained conditions (i.e., the product of the strain rate and the Darcy timescale $Da = t_D\varepsilon = \mu_f L^2/(k\Delta P)$ is much less than unity, Heap & Wadsworth, 2016).

During all tests, a linear variable differential transformer (LVDT) monitored the position of the upper piston with an accuracy of 0.2 μm, thus giving access to displacement, and a pressure probe in the axial pressure circuit provided a measurement of the applied axial force. Using the initial dimensions of the sample, axial stress and strain were obtained. Porosity change was provided by the conversion of the pore volume change given by the displacement of the piston in the pore pressure intensifier (the system was calibrated to take into account the compressibility of the pore fluid (water)). Finally, acoustic emission (AE) activity was recorded using a USB AE Node from Physical Acoustics and a piezoelectric transducer (a micro80 sensor from Physical Acoustic with a bandwidth of 200–900 kHz) attached to the lower piston. AE activity was monitored using the software AEwin and we set the detection threshold for an AE hit at 28 dB. The AE energy is determined by AEwin as the area under the received waveform. Experiments were stopped after the samples were unloaded at the same servocontrolled rate as loading and the pressures removed slowly so as not to damage the samples. For experiments conducted in the brittle regime, samples were unloaded following macroscopic failure. In the ductile regime, samples were deformed up to a 4% axial strain if mechanical data indicated strain localization (i.e., if there were small stress drops in the mechanical data) and up to 6% if not. Based on previous studies on natural rocks (Baud et al., 2004), these strains are considered suitable for subsequent observation of microstructural deformation features. To gain insights into the microstructure, polished thin sections were prepared using selected deformed samples and micrographs of the thin sections were obtained using a SEM.

4. Mechanical Data

In this study, compressive stress and compactive strain, that is, shortening for axial strain and decreasing volume for volumetric strain, will be conventionally taken as positive. The maximum and minimum applied principal compressive stresses are referred to as σ_1 and σ_3, respectively, the differential stress as $Q = \sigma_1 - \sigma_3$ and the effective mean stress as $P = (\sigma_1 + 2\sigma_3)/3 - P_p$.

4.1. Results of the Hydrostatic and Triaxial Tests

Representative data for the mechanical response of sintered glass bead samples to hydrostatic loading are presented in Figure 2. The hydrostatic experiment was conducted on a synthetic sample with a porosity and mean grain diameter of 0.38 and 0.2 mm (3714 in Table 2) and the mechanical data are plotted alongside the corresponding AE activity (dashed purple). The gray dashed curve in Figure 2 presents the mechanical data from an experiment performed on a sample with a very similar porosity and the same grain diameter to show the reproducibility (3712 in Table 2). The porosity reduction in pourcentage corresponds to the absolute loss of porosity. In Figure 2, the hydrostats present the following characteristic phases. (1) The initial evolution of porosity with increasing effective pressure is nonlinear. The duration of this first stage varies from sample to sample, as demonstrated by the difference between the black and the gray curves,

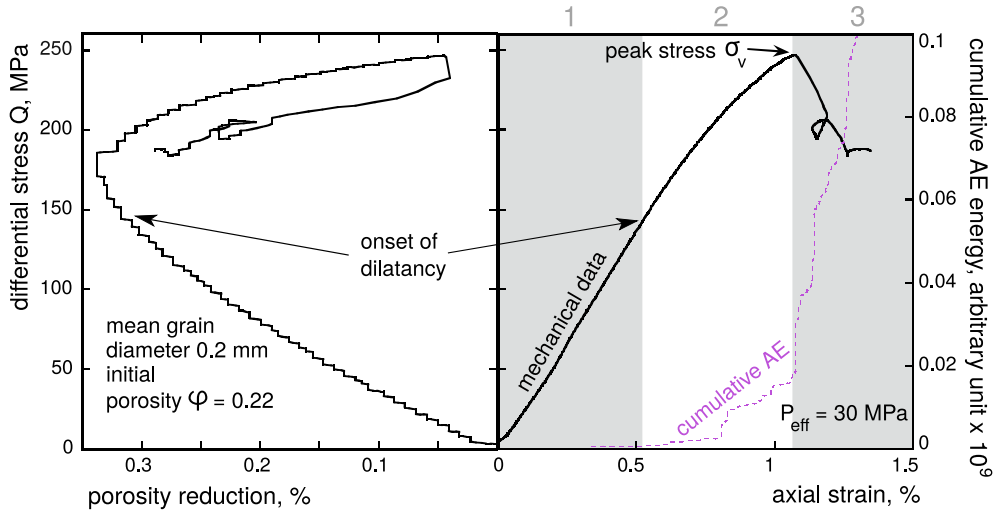

Figure 3. Representative mechanical data (black lines) and cumulative acoustic emission energy (purple dashed line) for triaxial tests performed in the brittle regime. The triaxial test presented was performed at P_{eff} = 30 MPa on a synthetic sample of mean grain diameter of 0.2 mm and initial porosity of 0.22. The peak stress σ_v is indicated by an arrow. The porosity reduction in percentage corresponds to the absolute loss of porosity, that is, a porosity reduction of 0.4% refers to a drop from 0.22 to 0.216. (1) When loading is first applied, the sample undergoes elastic axial strain and porosity decreases linearly. (2) The transition to the inelastic stage of deformation takes place at the onset of dilatancy and, as Q is increased further, it eventually reaches (3) a critical peak stress σ_v at which point brittle failure takes place and the stress drops to a residual value.

and is positively correlated to porosity. (2) The second phase consists of a linear decrease of porosity as a function of increasing effective mean stress, which is characteristic of poroelastic behavior. Almost no AEs are recorded during the initial nonlinear and linear portions of the hydrostatic experiment (Figure 2). However, a sudden increase in cumulative AE, associated with a sharp breaking point in the mechanical data, indicated as P^*, marks the transition to (3) a third phase characterized by a large decrease in porosity (of about 0.1) at constant effective pressure. For siliciclastic rock, this inflection on the hydrostat followed by a large porosity reduction is characteristic of inelastic compaction by delocalized grain crushing (Zhang et al., 1990), P^* therefore represents the critical stress for the onset of grain crushing. After equilibrium of the system has been reached for the critical state of stress P^*, further increase of the effective stress is accompanied by hardening. Samples submitted to hydrostatic loading (up to the maximum capability of the pressure cell; i.e., P_c = 200 MPa) presented effective pressure-porosity reduction curves similar to the hydrostats presented in Figure 2.

Triaxial compression experiments were conducted at effective pressures P_{eff} ranging from 20 to 180 MPa and, depending on the effective pressure P_{eff}, led to either brittle or ductile failure. A representative curve for the mechanical data and AE activity corresponding to failure by dilatancy and shear fracture formation (i.e., brittle behavior) is presented in Figure 3. The stress-strain curve can be divided into three parts. (1) First, the axial strain increases linearly with the differential stress and very few AEs are recorded. (2) Second, a sudden increase in the AEs accompanies a small decrease in the slope of the stress-strain curve, which corresponds to the onset of dilatancy (Figure 3). (3) Finally, as the AE bursts, the differential stress reaches a peak (marked as σ_v) and then drops to a residual value. Among the synthetic samples deformed under triaxial conditions, samples of porosity below 0.26 demonstrated brittle behavior up to effective pressures of 30–60 MPa, depending on their grain diameter. The peak stresses σ_v for samples deformed in the brittle regime are compiled in Table 2.

Figure 4 shows the third type of mechanical data obtained in this study, that is, mechanical data for triaxial tests conducted on synthetic samples at relatively high confinement and which failed by shear-enhanced compaction. In Figure 4, the stress-strain curve can be delimited into two main portions. (1) As we first load the sample, axial strain increases linearly with differential stress and no AEs are recorded. (2) Then, a subtle decrease in the slope of the stress-strain curve takes place as the AEs start to increase at the onset of

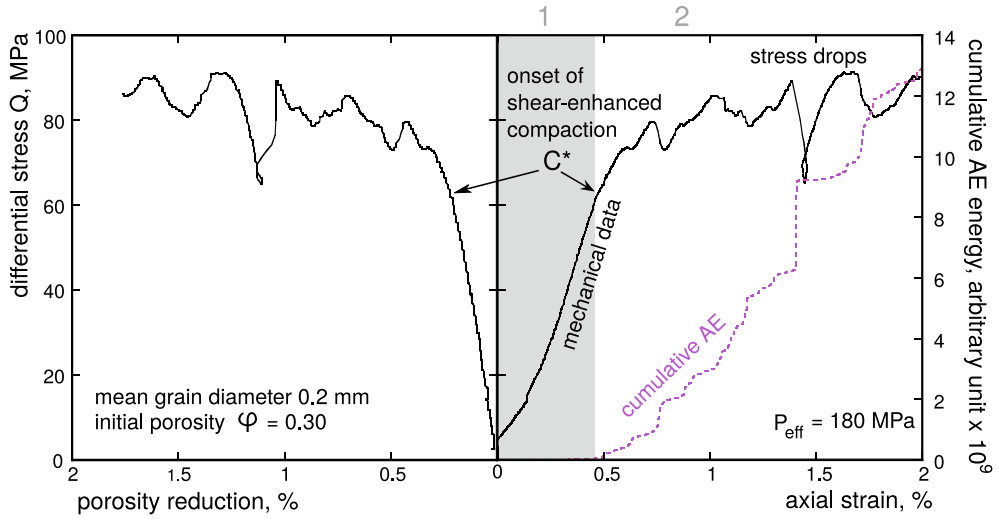

Figure 4. Representative mechanical data (black lines) and cumulative acoustic emission energy (purple dashed line) for triaxial tests performed in the regime of shear-enhanced compaction. The triaxial test presented was performed at P_{eff} = 180 MPa on a synthetic sample of mean grain diameter of 0.2 mm and initial porosity of 0.30. The critical stress for the onset of shear-enhanced compaction C^* is indicated by an arrow. The porosity reduction in percentage corresponds to the absolute loss of porosity, that is, a porosity reduction of 2% refers to a drop from 0.30 to 0.28. (1) Axial strain increases and porosity decreases linearly as loading is first applied. (2) The transition to the inelastic stage of deformation takes place as Q reaches the critical value C^* for the onset of shear-enhanced compaction.

shear-enhanced compaction C^* (Wong et al., 1997). Finally, the stress-strain curve reaches a plateau punctuated by stress drops that correlate to spikes in the AEs. These stress drops are suggestive of the formation of compaction bands (Baud et al., 2004). All samples deformed in the range of effective pressures corresponding to shear-enhanced compaction demonstrated such stress drops, sometimes accompanied by strain hardening. The critical stresses C^* for samples deformed in the ductile regime are compiled in Table 2.

An overview of the mechanical data collected for this study is presented in Figure 5. Mechanical data for triaxial experiments are compiled with their corresponding hydrostatic pressurization curves, for samples of porosity ranging from 0.18 to 0.38 and for mean grain diameters of 1.15 (blue), 0.5 (green), and 0.2 (orange) mm. At low and high effective pressures, the mechanical data present the phases described for Figures 3 and 4, respectively. The mechanical data for triaxial compression follow the hydrostat in the poroelastic domain. The deviation from the hydrostat marks the transition to inelastic deformation, either by dilatancy (increase in porosity) or by shear-enhanced compaction (porosity reduction). Some samples deformed in a mode that cannot be easily defined as "brittle" or "ductile," The mechanical data for the experiments performed at effective pressures of 30, 60, and 90 MPa in Figure 5c are representative of this hard-to-define failure mode, which we will refer to as transitional. For all the experiments, peak stresses and critical stresses were identified to map out the failure envelopes of our synthetic samples (Table 2).

4.2. Critical Stress States: Effect of Porosity and Grain Size

For all experiments, critical stress values were identified in accordance with the failure mode (Figures 2–4). Regarding experiments conducted in the brittle and transitional regime, critical stresses P and Q were, respectively, identified at the peak and at the first stress drop. For experiments conducted in the ductile regime, the stresses P and Q were identified at the deviation from the hydrostat, that is, at the onset of shear-enhanced compaction C^* (Figure 5). Table 2 includes all experiments for which the critical stresses could be clearly identified using mechanical data and AE measurements.

When plotted in the effective mean stress P, differential stress Q space, peak stresses map out the brittle failure envelope (open symbols) and C^* values map out the compactive yield envelope (solid symbols). When it could be measured, P^* anchors the yield envelope on the x axis (P^* could not be measured for all combinations of porosity and grain size due to the pressure limitations of the triaxial press). The experiments

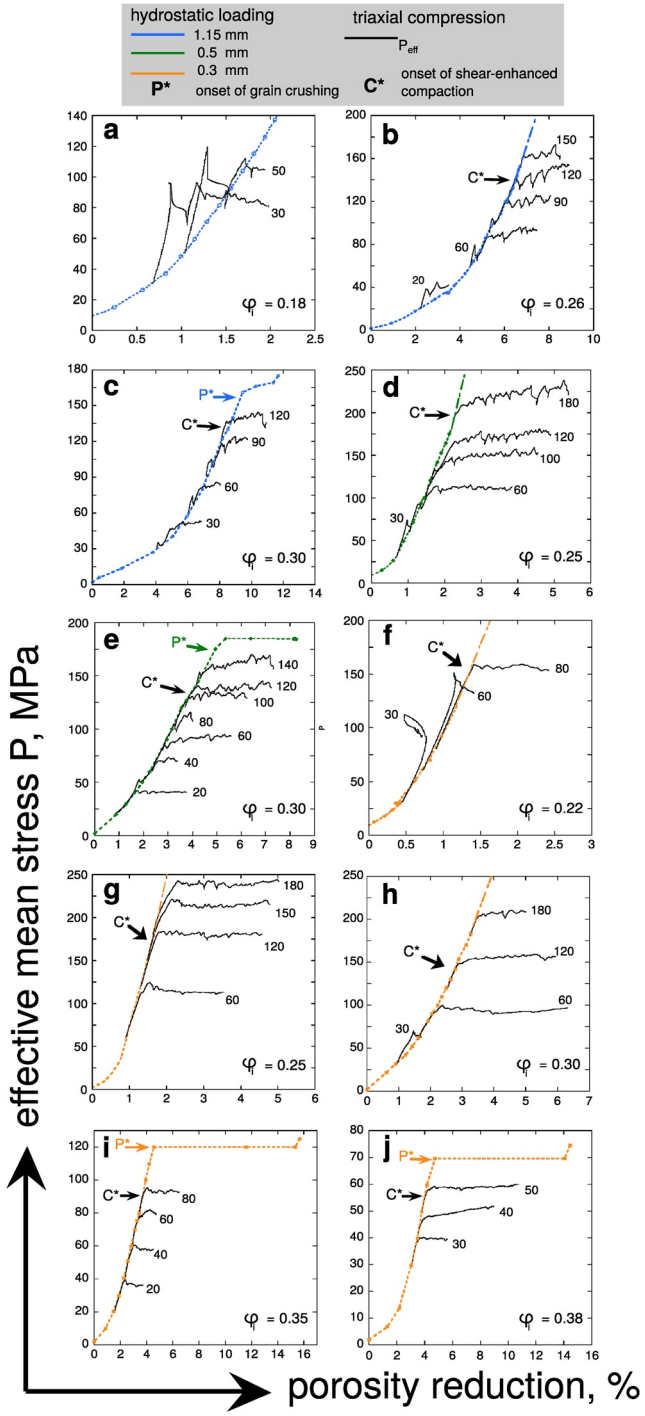

Figure 5. Compilations of mechanical data from hydrostatic loading (dashed colored) and triaxial tests (black) for samples with a mean grain diameter of 1.15 mm (blue) and an initial porosity of (a) 0.18, (b) 0.26, and (c) 0.30; a mean grain diameter of 0.5 mm (green) and an initial porosity of (d) 0.25 and (e) 0.30; and a mean grain diameter of 0.2 mm (orange) and an initial porosity of (f) 0.22, (g) 0.25, (h) 0.30, (i) 0.35, and (j) 0.38. Effective pressures at which triaxial tests were conducted are indicated at the end of the corresponding curves. The onset for inelastic deformation corresponds to the departure of the effective mean stress – porosity reduction curve from the hydrostat. For illustration, the onset of shear-enhanced compaction is indicated as *C** by black arrows. The critical stresses *P** for the onset of grain crushing are indicated by colored arrows on the hydrostats.

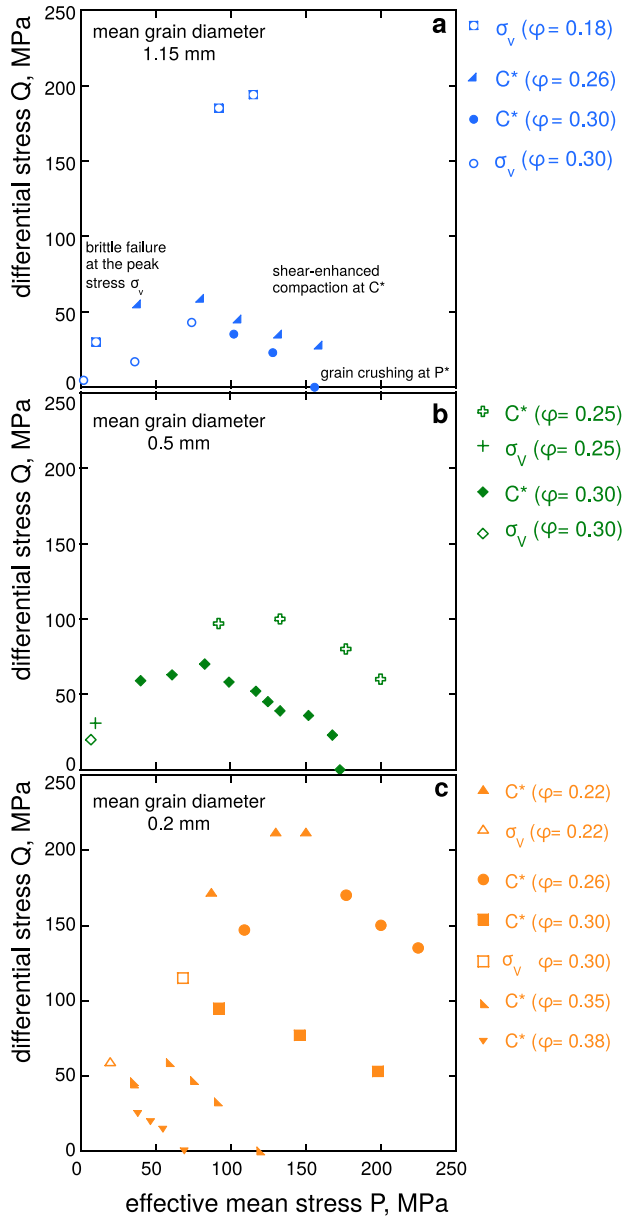

Figure 6. Compilations of failure envelopes for synthetic samples of mean grain diameter of (a) 1.15 mm, (b) 0.5 mm, and (c) 0.2 mm. Initial porosity of the synthetic samples is indicated in the legend. Failure envelopes are mapped out by critical stresses σ_v (brittle triaxial test), C^* (ductile triaxial test) and P^* (hydrostatic test). Open symbols correspond to peak stress values and solid symbols to C^* values. P^* (also a solid symbol) anchors the envelope to the x axis.

that exhibited a transitional failure mode exist where the brittle envelope meets the yield cap. Figure 6 presents a compilation of failure envelopes for our synthetic samples. Overall, several common features of the envelopes should be noted. First, brittle failure of these porous materials is restricted to a small area of the stress space. Second, regarding compactive yield caps, P and Q are linearly correlated, which is particularly clear for the caps in Figure 6c. Third, shear-enhanced compaction occurs over a wide range of stress states. For a given grain diameter, porosity is seen to influence compactive yield behavior. Broadly speaking, the higher porosity, the lower the stress that required for inelastic yield. For example, samples of mean grain diameter of 1.15 mm (Figure 6a) submitted to triaxial compression under an effective pressure of 120 MPa yielded at 23 and 35 MPa of differential stress for initial porosities of $\varphi = 0.30$ and $\varphi = 0.26$, respectively. For samples of mean grain diameter of 0.5 mm (Figure 6b), triaxial compression under an effective pressure of 100 MPa resulted in critical differential stresses of 100 MPa for $\varphi = 0.26$ compared to 52 MPa for $\varphi = 0.30$. Finally, for synthetic samples of mean grain diameter of 0.2 mm (Figure 6c) deformed at $P_{eff} = 60$ MPa, inelastic yielding took place at 223 MPa when $\varphi = 0.22$, 147 MPa when $\varphi = 0.26$, 95 MPa when $\varphi = 0.30$, and 42 MPa when $\varphi = 0.35$. In summary, increasing the porosity from 0.22 to 0.35 decreased the stress required for C^* by more than a factor of five (Table 2).

All else being equal, grain diameter also exerts an important influence on the compactive behavior. Figures 7a and 7b present a compilation of caps for $\varphi = 0.30$ and 0.25–0.26, respectively, for three different mean grain diameters (1.15 mm in blue, 0.5 mm in green, and 0.2 mm in orange). For $\varphi = 0.25$–0.26 and $P_{eff} = 60$ MPa, shear-enhanced compaction started at 59, 97, and 147 MPa for monodisperse samples of 1.15, 0.5, and 0.2 mm of mean grain diameter, respectively. For $\varphi = 0.30$ and $P_{eff} = 120$ MPa, C^* was reached at 23, 39 and 77 MPa for samples of 1.15, 0.5, and 0.2 mm of mean grain diameter respectively. In summary, increasing the mean grain diameter from 0.2 to 1.15 mm decreased the stress required for C^* by more than a factor of two (Table 2).

5. Microstructural Observations

Representative SEM micrographs for the microstructure of a synthetic sample after hydrostatic compression to beyond P^* are presented in Figure 8. The images correspond to a sample with an initial porosity and mean grain diameter of 0.357 and 0.2 mm (sample 3312; see Table 2), respectively, deformed up to a porosity reduction of 0.16. The corresponding mechanical data are presented in Figure 5i. At the lowest magnification, the thin section shows extensive delocalized grain crushing. Zooms into the microstructure confirm that most grains were entirely crushed and that the resulting shards progressively filled the porosity as the sample compacted. Uncrushed glass beads allow for the observation of cross-cutting microfractures propagating from grain to grain. On the basis of 2D image analysis (using ImageJ), the local final porosity was estimated. The least and most damaged areas yielded porosity values around 0.30 and 0.11, respectively.

Representative SEM for the microstructure of a synthetic sample triaxially deformed to beyond C^* are presented in Figure 9. The images correspond to a sample with an initial porosity and mean grain diameter of 0.35 and 0.2 mm (sample 3314; see Table 2), respectively, triaxially deformed at an effective pressure of 80 MPa up to an axial strain of 3.5%. The corresponding mechanical data are presented in Figure 5i. As

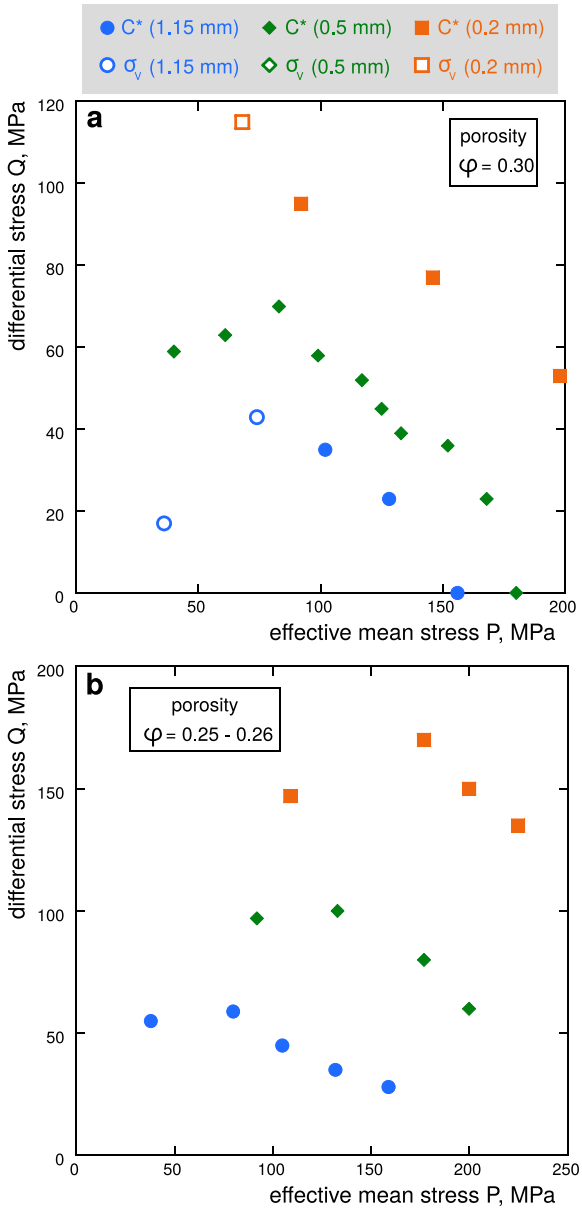

Figure 7. Compilations of failure envelopes for synthetic samples with a porosity of (a) 0.30 and (b) 0.25. Mean grain diameter of the synthetic samples is indicated in the legend. Failure envelopes are mapped out by critical stresses σ_v (brittle triaxial test), C^* (ductile triaxial test) and P^* (hydrostatic test). Open symbols correspond to peak stress values and solid symbols to C^* values. P^* (also a solid symbol) anchors the envelope to the x axis.

suggested by the small stress drops punctuating the stress-strain curve beyond C^* and the corresponding bursts of AE activity (Figure 5i), the sample contains evidence of compaction localization. Several discrete bands were observed in the upper and lower parts of the thin section, that is, at the extremities of the sample, and one cross-cutting discrete band was observed in the middle (Figure 9). The compaction band in the middle is 2–5 grains wide, that is, thickness of 0.4–1 mm, and is oriented normal to the direction to the maximum principal stress σ_1. Note that the band appears to avoid the porosity patches, and thus slaloms between them. A zoom on the band shows extensively fractured and compacted glass beads (Figure 9). Shards resulting from the fracturing and crushing fill the porosity within the band, reducing the porosity from 0.35 to approximately 0.27 (estimation based on 2D measurements on the SEM images using ImageJ). The grains are unaffected outside the compaction band, and the porosity was estimated using ImageJ to be similar to that measured in the laboratory (0.36).

6. Discussion

6.1. Suitability of Sintered Glass Beads as Crustal Analogs

Synthetic granular rocks such as our sintered soda-lime silica glass beads provide a well-characterized two-phase medium for investigating mechanical processes in siliciclastic rock. Our motivation for using synthetic samples was to quantify the influence of individual microstructural parameters (e.g., porosity and grain diameter) on the mechanical behavior of granular rock by keeping all other parameters constant. In natural sandstones, for example, samples with different porosities may also be characterized by different grain and pore sizes and distributions. However, understanding the mechanical behavior of sandstones using fused glass bead synthetics hinges on the comparability of natural and synthetic sandstones. Before discussing the suitability of sintered glass beads as analogs for crustal rocks, we will briefly mention the differences between the microstructure of our synthetic samples and natural crustal rocks. First, the grain size distribution of all the synthetic samples is monomodal and closely clustered (Figure 1a). Natural sandstones, for example, can be characterized by polydisperse grain size distributions. Second, the grains in our synthetic samples are spherical and have identical physical and mechanical properties, while natural sandstones often contain nonspherical grains and different types of grains (e.g., quartz and feldspar). Finally, natural sandstones can contain cement (e.g., clay cement between grains). Our synthetic samples do not contain cement (Figures 1c and 1d). To compare our synthetic samples to natural sandstones, we selected sandstones whose porosity and grain diameter lie in the range covered by our synthetic samples (our porosity range is 0.18–0.38 and our grain diameter range is 0.2–1.2 mm). We chose Boise sandstone (porosity of 0.35 and average grain radius 0.46 mm; Bedford et al., 2019; Zhang et al., 1990), Idaho Gray sandstone (porosity of 0.36 and average grain radius 0.7 ± 0.2 mm; Bedford et al., 2019) and Bentheim sandstone (porosity of 0.23 and average grain radius 0.3 mm; Klein et al., 2001). Bentheim sandstone is a monomineralic sandstone with a narrow grain size distribution. Due to its homogeneous mineralogy and well-sorted grain size, it has been used in many rock deformation studies, notably on strain localization (Baud et al., 2004; Tembe et al., 2006, 2008; Wong et al., 2001). It is therefore an ideal sandstone to compare with our synthetic samples. We compiled mechanical data from hydrostatic and triaxial experiments conducted in conditions similar to those imposed during experiments on the synthetic samples, that is, at room temperature on water-saturated samples at a fixed pore pressure of 10 MPa. In

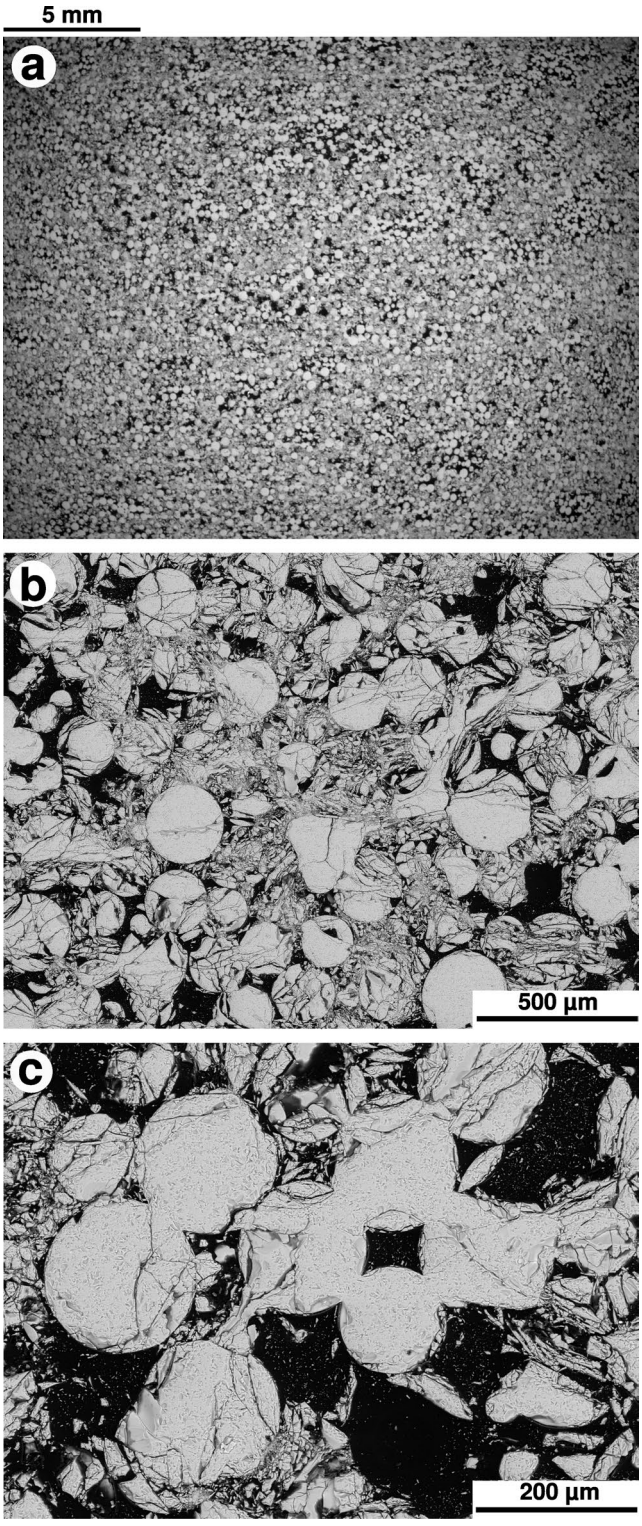

Figure 8. Representative scanning electron micrograph of the (a) microstructure of a synthetic sample deformed under hydrostatic loading up to an effective stress beyond P^*. (b, c) Zooms in showing extensive grain crushing. Black: porosity, gray: glass.

Figure 10, we plot selected mechanical data from our database alongside mechanical data from hydrostatic experiments (a) and triaxial experiments (b) conducted on Boise, Idaho Gray and Bentheim sandstones.

Regarding the hydrostatic behavior (Figure 10a), we first note that, during the initial loading and increase of the effective pressure up to P^*, Boise, Idaho Gray, and the synthetic sample with a porosity of 0.35 present porosity reduction curves that are almost identical. The characteristic "tail" at the beginning of the hydrostat is typically attributed to the closure of microcracks (Walsh, 1965). Assuming our sintered glass beads do not contain microfractures at the beginning of the hydrostatic pressurization, as indicated from our microstructural analysis of the intact material, we attribute the nonlinear initial portion of the hydrostat to grain rotations and rearrangements, which is corroborated by the positive correlation between the size of the tail (i.e., the amount of compaction) and the porosity of the sample. Qualitatively speaking, the compaction curves evolve differently beyond P^*. While a progressive inflection and strain hardening is observed for both Boise and Idaho Gray sandstones, P^* manifests as a sharp breaking point beyond which the synthetic sample undergoes a porosity reduction of about 0.1 without hardening. Zhang et al. (1990) demonstrated that the first inflection in the hydrostat corresponds to the inception of grain crushing and that increasing the effective pressure beyond this point exacerbates the deformation. This gradual behavior is absent for the synthetic sample, which experiences extensive grain crushing and porosity loss at the state of stress just higher than P^*. The observation of extensive grain crushing at a stress just above P^* is similar to that reported for Bentheim sandstone, a rock that also contains a closely clustered monomodal grain size distribution (Baud et al., 2006) (Figures 10a and 10c). Examination of the microstructure showed that very few areas in the sample remained uncrushed (Figure 8). Contrary to most natural sandstones (e.g., Caruso et al., 1985), our synthetic rocks are composed of monomodal distributions of uniform grains of identical elastic properties. Thus, the force chains induced in the granular framework during loading are expected to be more homogeneously distributed in our monodisperse synthetic samples (Guéguen & Boutéca, 2004; Papadopoulos et al., 2018). As a result of this homogeneity, when the externally applied effective pressure reaches the critical value P^*, the normal forces induced at the grain contacts must reach the critical value at the same time, and most grains are thus crushed at the same state of stress. Quantitatively, the effective stress at which the onset of grain crushing (P^*) occurs is higher in our synthetic rock (120 MPa) than it is in Boise (75 MPa) and Idaho Gray (55 MPa) sandstones. Several differences between the synthetic and natural samples could be considered to explain the higher P^* in the synthetic samples. First, Boise and Idaho Gray sandstone have a larger average grain diameter. Second, Boise and Idaho Gray sandstone contain minerals other than quartz that are characterized by lower values of fracture toughness, such as feldspar (Atkinson & Meredith, 1987). However, although the mineral composition of the two sandstones is very close, the P^* of Boise sandstone is about 25 MPa higher than that of Idaho Gray sandstone (Figure 10a). Therefore, we speculate that the much higher P^* for the synthetic samples could arise from the difference in grain diameter (the smaller the grains, the stronger the sample).

We will now compare the behavior of natural sandstones with the one of our synthetic samples when subject to triaxial compression. Figure 10b

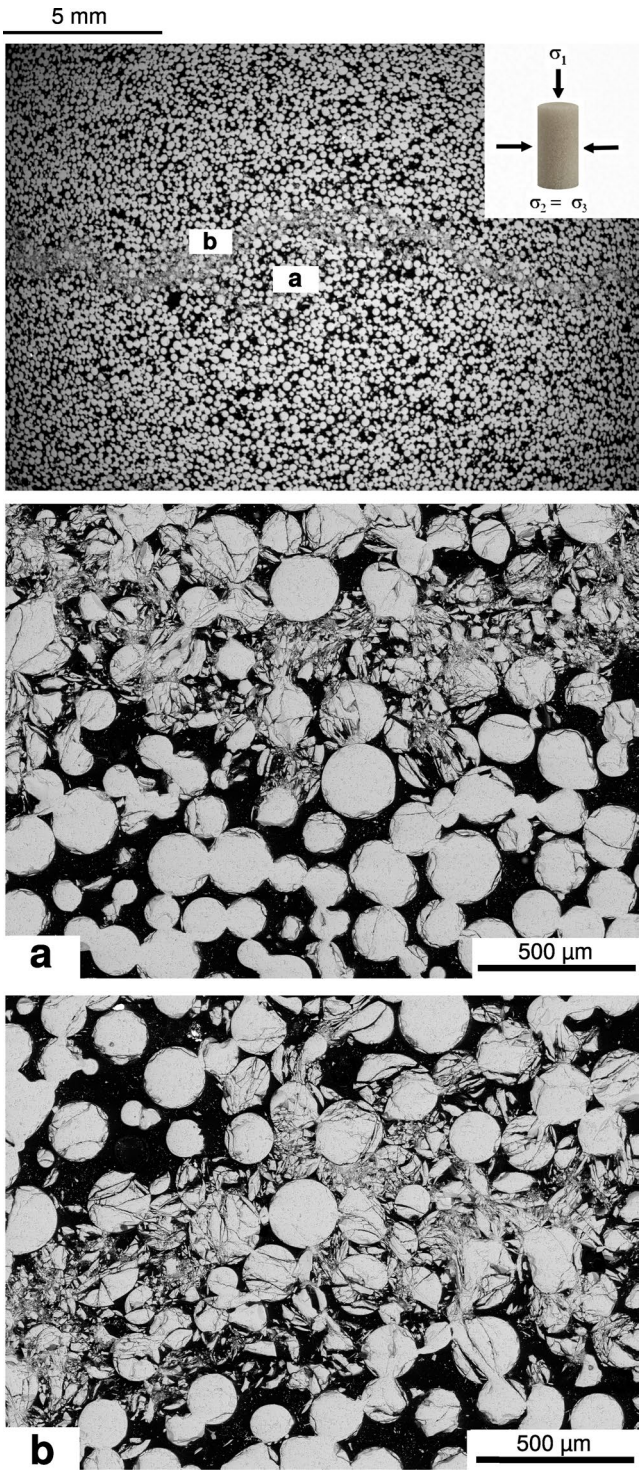

Figure 9. Scanning electron micrograph of the microstructure of a synthetic sample that failed by development of discrete compaction bands. Sample 3314, with a porosity of 0.35 and a mean grain diameter of 0.2 mm, was deformed under 80 MPa (Table 2). Overview of the thin section allows for the observation of a discrete compaction band in the middle, formed in a direction normal to the maximum principal stress σ_1. (a) and (b) show micrographs of a discrete 2–5 grain-thick band within which most grains are crushed. The microstructure outside of the band is almost intact. Black: porosity, gray: glass.

presents mechanical data from triaxial tests conducted on a synthetic sample with a porosity of 0.3 (orange line) and on Bentheim sandstone (Baud et al., 2004) (black line) under an effective pressure of 120 MPa. Qualitatively, the stress-strain curves are very similar. Quantitatively, C^* is about 50 MPa higher in Bentheim sandstone than in the synthetic sample and is likely the result of the difference in porosity and grain size (both higher for the synthetic sample). Beyond C^*, the mechanical data for both samples show small stress drops, suggesting that the samples failed by development of compaction localization, as shown by Baud et al. (2004).

Although studies on the mechanical behavior of tuffs under hydrostatic and triaxial compression are comparatively rare (e.g., Heap, Kennedy, et al., 2015; Zhu et al., 2011), our new data for sintered synthetic samples are also relevant to welded granular materials. Indeed, in the case of welded tuffs, the product of the deposition of hot volcanic ash and lapilli, our samples are an exact analog, where volcanic welding and glass sintering are fundamentally the same dynamic process (Wadsworth et al., 2019). We note that in nature, welding of tuff can be associated with internally porous clasts, vesiculation or resorption, viscosity or temperature gradients, and shear, all of which can conspire to complicate microstructure relative to sintered glass beads, but that nevertheless, the broad theme of mechanical results given here are relevant in volcanic environments as well as other crustal scenarios.

6.2. Deconvolution of Microstructural Parameters

In nature, porosity is often related to grain diameter. However, numerous other parameters such as grain sorting, shape, orientation, location of cements, and the extent of compaction, can influence the bulk porosity of a porous rock (Rogers & Head, 1961; Scherer, 1987). One of the results of this multi-component control on porosity is that crustal rocks that show a low porosity are not necessarily composed of small grains and vice versa. In fact, crustal rocks span a wide range of porosity-grain size combinations and can demonstrate complex porosity-grain size relationships. For illustration, we have compiled the porosity and the mean grain diameter of 19 natural sandstones that have repeatedly been used in laboratory studies (Figure 11). Porosity values are in the range 0.03–0.38 and mean grain diameter values are in the range 0.075–0.92 mm. If we consider only this subset of natural sandstones, several observations can be made: (1) for the few sandstones with a porosity higher than 0.25, the mean grain diameter varies over a range twice as large as sandstones of lower porosity (0.2–0.9) and (2) for sandstones of porosity lower or equal to 0.25, mean grain diameter is lower than 0.5 mm and clusters around 0.28 mm; such that the grain size effect on porosity becomes attenuated as diagenesis progresses as pore and pore throats are compacted. By compiling these data, we can conclude that (3) sandstones that come from a single formation (see, e.g., Buntsandstein, Fontainebleau or Boise sandstones) can cover a large range in grain diameter and porosity, within which variations in grain diameter appear to occur independently from variations in porosity and vice versa. For example, the porosity of Fontainebleau sandstone can vary greatly (0.03–0.28), while the mean grain diameter (0.250 mm) remains constant (Bourbie & Zinszner, 1985; Lindquist et al., 2000; Louis et al., 2007). It is important to note that there is some bias in sample selection for laboratory studies, such that crustal rocks with a low variability within a unit are favored so that repeat measurements can be made (e.g.,

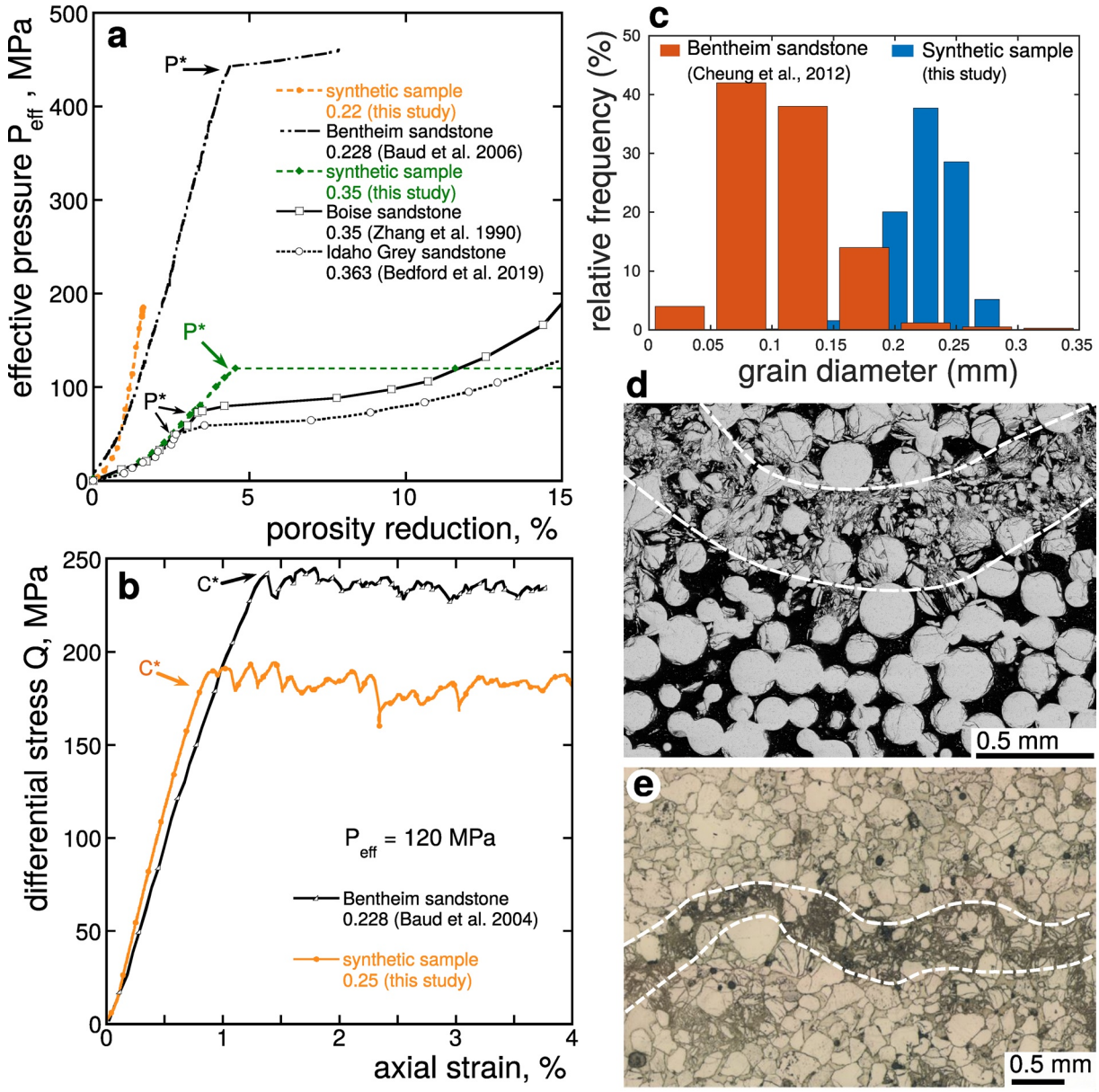

Figure 10. Data from tests performed on synthetic samples compared to data for sandstones from the literature. (a) Comparison of the hydrostatic loading curve of a synthetic sample (green dashed) with a porosity of 0.35 and a mean grain diameter of 0.5 mm and of the hydrostatic loading curve of a synthetic sample (orange curve) with a porosity of 0.22 and a mean grain size of 0.2 mm, with the hydrostat of Boise sandstone (black line), with a porosity of 0.35 and a mean grain diameter of 0.92 mm (Zhang et al., 1990), the hydrostat of Idaho Gray sandstone (dashed black) with a porosity of 0.363 and a mean grain diameter of 0.7 mm (Bedford et al., 2019) and the hydrostat of Bentheim sandstone with a porosity of 0.228 and a grain diameter of 0.3 mm (Baud et al., 2006). The onset of grain crushing is indicated as P^*. (b) Comparison of stress-strain curves obtained during a triaxial test at an effective pressure of 120 MPa performed on a synthetic sample (orange line) with a porosity of 0.25 and a mean grain diameter of 0.2 mm and on Bentheim sandstone (black line) (Baud et al., 2004). The onset of shear-enhanced compaction is indicated as C^*. (c) For reference, the smallest grain size distribution used in this study is presented along the grain size distribution of Bentheim sandstone (data from Cheung et al., 2012). (d) Comparison of a scanning electron micrograph of a discrete compaction band observed in a synthetic sample ($\varphi = 0.35$) and (e) an optical microscope image of a discrete compaction band in Bentheim sandstone ($\varphi = 0.23$; Baud et al., 2004).

Menéndez et al., 1996). We can find that field studies reported a much wider range of average grain size and porosity for sandstones, which can be encountered as very fine-grained (0.0625 mm; Selley, 2004) and can grade up to very coarse-grained and pebbly (2 mm; Selley, 2004), with well to poorly sorted distributions and porosity ranging over more than one order of magnitude 0.02–0.30 (e.g., Morrow, Nugget, Bartlesville, and Grimsby sandstone; Nelson & Kibler, 2003). For instance, anomalously high porosities were reported in

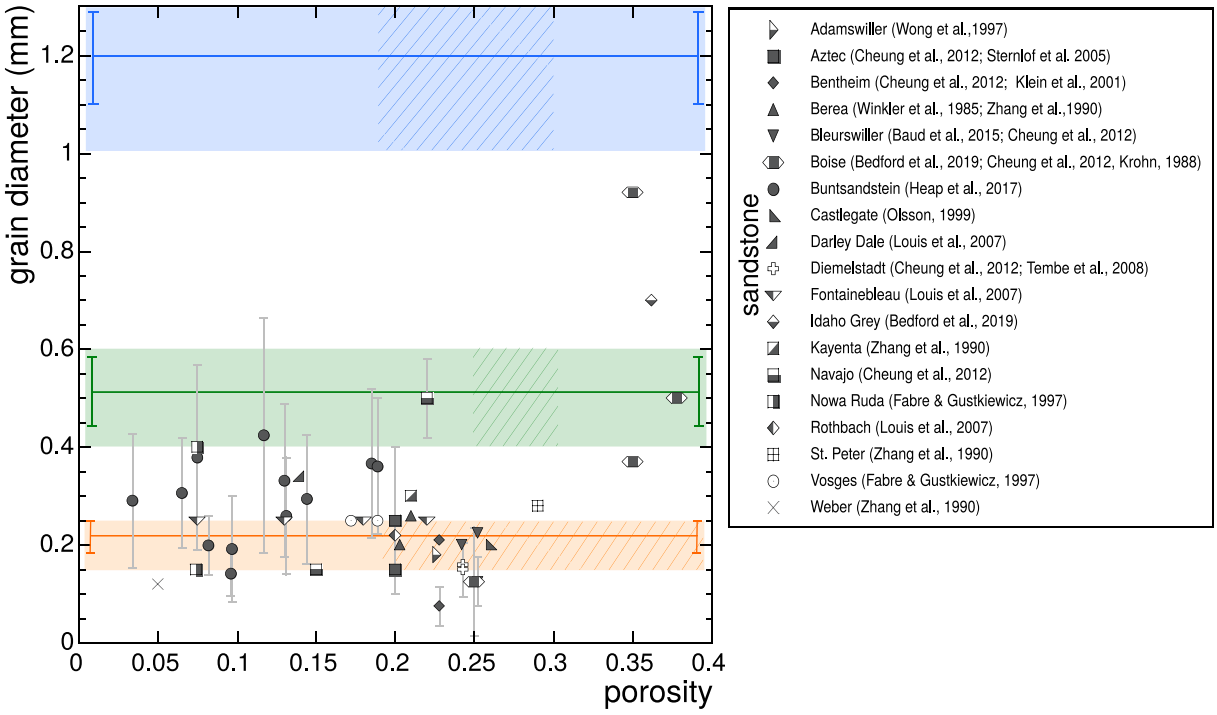

Figure 11. Compilation of porosity and grain diameter for laboratory sandstones (Baud et al., 2015; Bedford et al., 2019; Cheung et al., 2012; Fabre & Gustkiewicz, 1997; Heap et al., 2017; Klein et al., 2001; Krohn, 1988; Louis et al., 2007; Olsson, 1999; Sternlof et al., 2005; Winkler, 1985; Wong et al., 1997; Zhang et al., 1990). Colored areas correspond to the range of porosity-grain diameter accessible by sintering glass beads. The dashed areas correspond to the range we specifically investigated in this study. The error bars give the standard deviation of the grain diameter distribution, when it has been reported.

a significant number of deeply buried (>4 km) reservoir sandstones worldwide (e.g., porosity in the range 0.24–0.40 in the Tertiary channel-fill sandstone, offshore west Africa; Bloch et al., 2002).

Deconvolving structural parameters such as porosity and grain size is necessary to derive definitive constraints on the micromechanics of compaction from experimental studies. Indeed, while the importance of porosity in controlling yield strength is well-established for crustal rocks (e.g., Wong & Baud, 2012), the independent effect of a change of grain or pore size is only poorly investigated (Atapour & Mortazavi, 2018). As revealed when compiling grain diameter and porosity for laboratory sandstones (Figure 11), it is possible that the approximate consistency in the grain diameter has meant that its influence on compactive yield strength has been masked in rock mechanics study thus far. Sintering glass beads has allowed us to effectively deconvolve the effect of porosity and grain diameter and other microstructural factors, to parameterize specifically for their importance.

6.3. Influence of Porosity and Grain Size on Compactive Yield

Our synthetic samples were designed and prepared to maximize microstructural homogeneity. Yet, they present heterogeneities in the porosity distribution and in the geometry of grain-to-grain contacts (Figure 1). Similar porosity clusters have been reported in Bleurswiller sandstone, the mechanical compaction of which has been investigated in several studies (Baud et al., 2015; Fortin et al., 2005, 2006; Tembe et al., 2008). These published works have demonstrated the importance of porosity clusters on the micromechanical processes leading to inelastic compaction. Indeed, while yield envelopes reported for natural sandstones are typically elliptical in shape (Baud et al., 2006; Guéguen & Fortin, 2013; Wong et al., 1997), Bleurswiller sandstone presents an approximately linear yield cap (Baud et al., 2015). The linear yield envelope of Bleurswiller was fitted by Baud et al. (2015) using a dual-porosity micromechanical model for cataclastic pore collapse. The pore collapse model, initially developed for dual-porosity carbonates, treats the pore size distribution as bimodal with the pore space divided into microporosity and macroporosity (i.e., a porosity cluster) (Zhu et al., 2010). Assuming the matrix into which porosity clusters are embedded

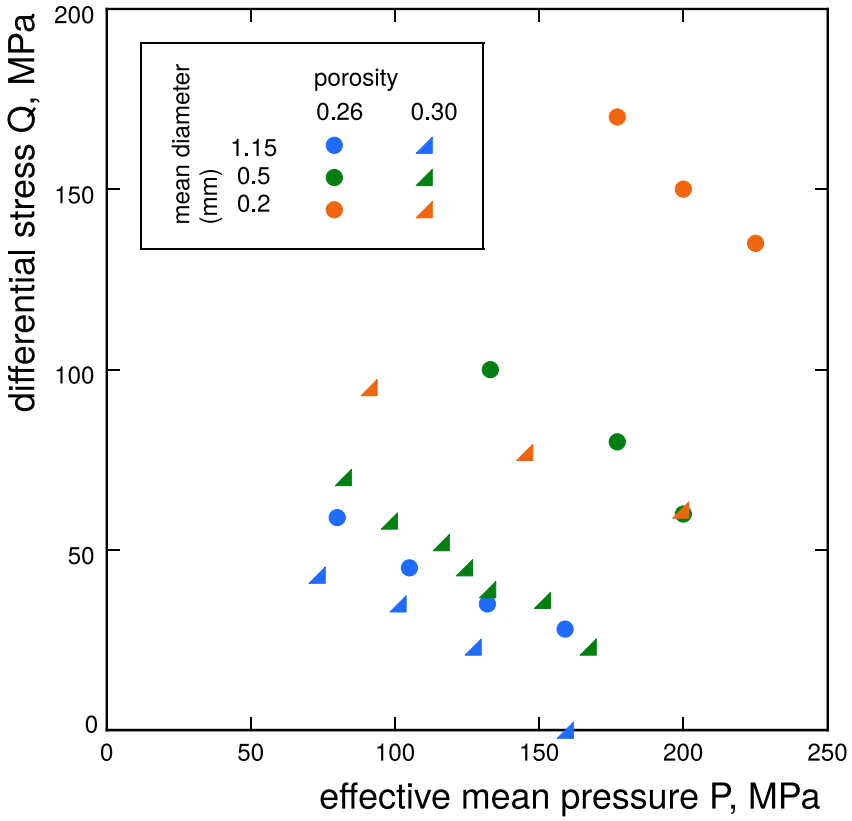

Figure 12. Influence of porosity on the compactive yield strength. Compactive yield envelopes for synthetic samples with a porosity of 0.26 (round solid symbol) or 0.30 (triangle solid symbol) and a mean grain diameter of 1.15 mm (blue), 0.5 mm (green) or 0.2 mm (orange) are compiled.

fails according to the Coulomb criterion, the pore collapse model predicts that a porosity cluster collapses when the stress field in its vicinity attains the critical state according to the Coulomb criterion, which results into a linear dependence of the differential stress Q at the yield point C^* with the effective stress P (Baud et al., 2015). Although our yield caps that include P^* appear linear, further microstructural analysis need to be done to identify the micromechanical process and clarify the role of pore collapse in the failure of our synthetic samples.

The pore space heterogeneities of our synthetic samples appear to influence the micromechanics of failure. Yet, we believe they do not prevent us from discussing the relative influence of bulk porosity on the compactive yield behavior. A compilation of six yield envelopes for synthetic samples of porosity of 0.25 and 0.30 and of mean grain diameter of 0.2, 0.5, and 1.15 mm is presented in Figure 12. All of the compactive yield caps are linearly shaped with a negative slope. Overall, we observed that, for a given grain diameter, increasing porosity decreases the stress at which C^* occurs and that a difference in porosity of 0.01 results in a difference in C^* of approximately 8% ± 5%. This appears to apply whatever the grain diameter is in the range 0.15–1.3 mm. Indeed, at an effective pressure of 60 MPa, an increase of porosity from 0.26 to 0.30 (+0.04), decreases the stress at which C^* occurs from 59 to 43 MPa (−28%), 97 to 70 MPa (−28%) and from 147 to 95 MPa (−35%) for mean grain diameter of 1.15, 0.5, and 0.2 mm, respectively.

As for porosity, grain size was experimentally identified to have a first-order control on compactive yield of porous siliciclastic rock (Wong, 1990; Wong et al., 1992, 1997; Zhang et al., 1990) and has been included as a parameter in micromechanical models (e.g., Sammis & Ashby, 1986; Zhang et al., 1990). In the Hertzian fracture model of Zhang et al. (1990), average grain radius acts as a scaling parameter for the critical pressure P^* with an equal weight than porosity. This model was successfully applied to a number of natural and synthetic sandstones and unconsolidated materials (David et al., 1998; Wong et al., 1997) with some scatter. However, although a consensus on the key influence of grain size has been reached, compactive yield caps

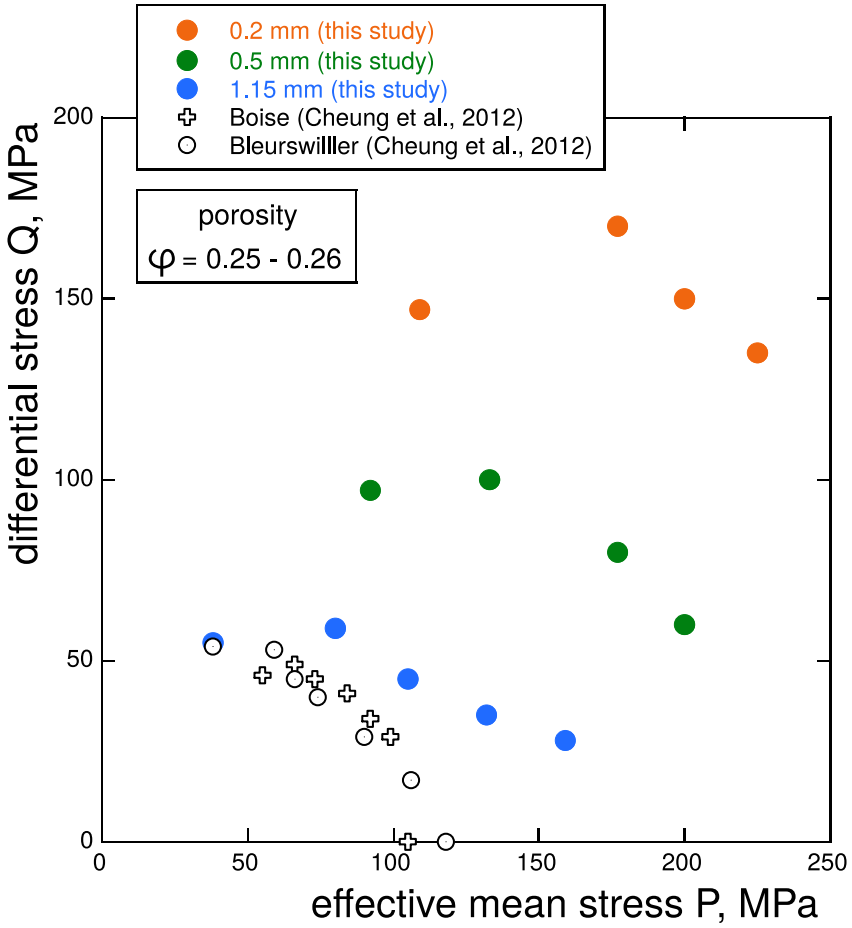

Figure 13. Influence of grain diameter on the compactive yield strength. Compactive yield envelopes for synthetic samples with a porosity of 0.25 and a mean grain diameter of 0.2 mm (orange), 0.5 mm (green), and 1.15 mm (blue) are compiled with yield envelopes for Boise (open cross) and Bleurswiller (open circle) sandstones (data from Cheung et al., 2012).

compilations for sandstones often only discuss the influence of porosity. Figure 13 shows a compilation of compactant failure caps for Boise and Bleurswiller sandstones (data from Cheung et al., 2012) and sintered samples that only differ from one another in terms of their average grain diameter. If we consider only the yield caps of the synthetic samples, we observe that, all else being equal, an increase in average grain diameter from 0.2 to 0.5 mm (+130%) or from 0.5 to 1.15 mm (+150%) shifts the stress at which C^* occurs to values approximately 2 times lower (−50%) (Figure 13). Moreover, the difference in C^* that results from a change in grain diameter remains approximately the same whatever the porosity. Thus, our data show that an increase in average grain diameter by a factor of 2 results in a decrease in the stress to reach C^* of approximately 50% ± 5%. As for Boise and Bleurswiller sandstone, they are similar in mineralogy and porosity but, although both their grain diameter distributions present a peak at 125 μm, the former has a wider sorting that extends up to 725 μm. Despite significantly different grain sorting, their compactive yield caps for the onset of shear-enhanced compaction are very similar, albeit slightly different in shape with a more linear cap for Bleurswiller sandstone. The caps of our synthetics are similar in shape to those of the natural sandstones but are mapped out at very different stress states (Figure 11). Tembe et al. (2008) reported that Bentheim sandstone, although similar to Boise and Bleurswiller sandstones in terms of porosity, presents a compactive yield cap characterized by higher stresses. Indeed, the abundance of secondary minerals (feldspar, oxide, and mica) in Boise and Bleurswiller compared to Bentheim (>99% quartz) likely causes the decrease in the compactive yield stresses for Boise and Bleurswiller sandstones. Similarly, since Bleurswiller and Boise sandstones present a grain diameter distribution with a peak at 125 μm, we would expect their compactive yield caps to be mapped out at higher stresses than the caps for the synthetic samples that have

grain diameter distributions with peaks at 200, 500, and 1,150 μm (Figure 13). The discrepancy in compactive yield stresses between Boise and Bleurswiller sandstones and the synthetic samples can be attributed neither to porosity nor to grain size, but possibly to the presence of cement and of secondary minerals other than quartz (feldspar, oxide, and mica).

Overall, we varied grain diameter by one order of magnitude (Figure 11) and we see a large effect of that variation on the yield compactive strength of our synthetic samples. Grain diameters of natural sandstones can also vary by more than one order magnitude (Nelson & Kibler, 2003), but the effect of that variation has not hitherto been deconvolved from other microstructural factors. We thus conclude that, if grain size were to be accounted for quantitatively, its effect would be similar to that of porosity. However, we observe, for the range of porosity and grain diameter used herein, that the influence of porosity on compactive yield is higher than the influence of grain diameter. Indeed, to cover a similar range in the stress space, the average grain diameter of our synthetic samples was increased by up to 600% (relative to the lowest range we used, 0.15–0.25 mm) while bulk porosity was only increased by up to 120% (relative to the lowest porosity we used, 0.18).

6.4. Compaction Localization

For all of our synthetic samples deformed in the regime of shear-enhanced compaction, mechanical data show stress drops of variable amplitude (Figure 5), suggesting that compaction localization took place (Baud et al., 2004; Heap, Brantut, et al., 2015; Louis et al., 2006). This observation concurs with the general consensus that microstructural homogeneity promote strain localization in granular materials (Katsman et al., 2005; Louis et al., 2009; Wang et al., 2005). Indeed, Cheung et al. (2012) demonstrated that uniform grain size distribution promotes the development of discrete compaction bands. As our synthetic samples are characterized by a monodisperse distribution of grain size, we expected compactant deformation to localize in the form of compaction bands. In Figures 10c and 10d, we juxtaposed a SEM micrograph of a discrete compaction band in a synthetic sample and a micrograph of a discrete compaction band in Bentheim (from Baud et al., 2004), respectively. The compaction bands present very similar microstructural attributes (Figures 10c and 10d). An important difference is that our micrograph has been obtained on a sample of porosity of 0.35. To our knowledge, the range of porosity over which compaction bands were reported in sandstones is approximately 0.13; 0.29 (Fossen et al., 2011; Schultz et al., 2010; Tembe et al., 2008). The mechanical behavior of sandstones with a porosity higher than 0.29 at or near the brittle-ductile transition has been studied (e.g., Bedford et al., 2019; Cheung et al., 2012; Wong et al., 1997) but high-porosity sandstones typically used in laboratory often have polydisperse distributions of grain size (see, e.g., Boise sandstone), which has been recognized to inhibit strain localization. Therefore, the effect of porosity on the propensity for compaction localization may have been masked by the influence of other structural parameters. Our new data therefore extend the upper limit of porosity for which compaction localization has been observed to 0.35 and suggest that compaction localization can occur in samples with a porosity up to 0.38 (the highest porosity of our set of samples).

However, although numerical simulations suggested compaction localization could occur in sand packs (Marketos & Bolton, 2009), experimental validation for the formation of compaction bands in high-porosity granular aggregates such as unconsolidated sands have not been reported. For example, Hangx and Brantut (2019) performed triaxial experiments on Ottawa quartz sand with a porosity of 0.36 and did not observe strain localization in the compactant regime of deformation. These authors proposed that the possibility for grain rotation and rearrangement, permitted by the lack of cementation, allows grain failure to be accommodated and prevents stress concentration to occur. Although our high-porosity synthetic samples do not have cement, we show that they can develop compaction bands in the regime of shear-enhanced compaction. Therefore, we speculate that the necks formed at grain contacts during sintering in our synthetic samples act as the cement in consolidated sandstones and play a key role in controlling compaction localization. To a first-order, the potential for compaction localization appears to be controlled not by porosity, but by the granular/nongranular and/or unconsolidated/consolidated nature of rock, which is intimately related to the degree of cementation at grain contacts and by extension, in some cases, to porosity (Lemée & Guéguen, 1996). Additionally, if we consider that the porosity of a loose packing of grains is approximately 0.38 ± 0.01 (Johnson & Plona, 1982), the observation of discrete compaction bands in a synthetic sample

of porosity of 0.35 suggests that even a small proportion of consolidated/cemented grain contacts could be sufficient to trigger stress concentrations within aggregates and the formation of compaction bands.

7. Crustal Implications and Concluding Remarks

Crustal rocks such as sandstones and tuffs, the primary microstructural elements of which are comparable with our synthetic samples, occur as geological units in reservoirs, aquifers, fault zones, and in volcanic environments; settings where they typically undergo structural changes due to geologic processes. Therefore, implications, and applications, of our results for natural systems are broad. For example, in the context of hydrocarbon and/or geothermal reservoirs, depletion-induced reservoir compaction is an ubiquitous phenomenon that eventually leads to surface subsidence (Gambolati et al., 2006; Nagel, 2001). On assessing which sedimentary layer compacts first and/or to the highest extent, unconsolidated upper formations and clay-rich formations are usually considered as the best candidates. However, reservoir formations are often only vaguely described as coarse-grained or fine-grained and grain size is rarely considered in numerical terms (Sun et al., 2018b), even in geotechnical models predicting the extent of irreversible compaction for the bulk reservoir (Buscarnera et al., 2020; Hol et al., 2018). Our new data suggest that formations with large grain diameters, alongside those with a high porosity, could be prime candidates for mechanical compaction and should therefore be considered when assessing reservoir subsidence.

In volcanic contexts, inelastic compaction of edifice-forming rock (including nonvolcanic basement rocks) presumably acts as a driving force in the growth and destruction life-cycle of large volcanoes (Bakker et al., 2015; Concha-Dimas et al., 2005; Heap, Farquharson, et al., 2015; Van Wyk De Vries & Borgia, 1996), which involves episodes of spreading that eventually leads to catastrophic collapses (Van Wyk De Vries & Francis, 1997). Since flank and/or edifice collapse models often invoke a weak/ductile internal or basal unit to explain instability and collapse (Ablay & Hürlimann, 2000; Morgan & McGovern, 2005; Voight, 2000), it is important to understand what controls the mechanical behavior of porous rocks, especially considering that porous volcanic rocks can also develop compaction bands (Heap, Kennedy, et al., 2015, 2020). Our synthetic materials could help understand whether simple empirical or theoretical models can effectively describe the relationship between grain size, porosity and compactive yield strength, and thus give accurate predictions for the evolution of inelastic compaction and subsequent subsidence and/or edifice spreading. Moreover, since our synthetic samples consist of a very simplified two-phase medium, such laws can be easily tested against discrete element method simulations of reservoir compaction (Alassi et al., 2006; Sun et al., 2018a) or volcanic collapses (Harnett et al., 2018) for example.

Our approach has allowed us to study the influence of deconvolved microstructural attributes on mechanical compaction. The set of mechanical and microstructural data we present show that the failure mode of analog samples made of sintered glass beads transit from brittle at low confinement to ductile with shear-enhanced compaction at high confinement. Compactive yield caps are mapped out on a range of stress states comparable to those for natural crustal rocks (the porosity and grain diameter of which are similar to those of our synthetic samples, that is, 0.18–0.38 and 0.2–1.15 mm, respectively) and are linearly shaped when P^* is known and are likely linearly shaped for the porosity-grain diameter combinations for which P^* could not be measured (due to the pressure limit of the triaxial apparatus). Qualitatively speaking, mechanical and microstructural data are very similar between the natural and synthetic samples. Regarding the influence of porosity and grain size, we arrived at the following main conclusions. First, increasing only porosity or only grain diameter decreases the stress at which the onset of shear-enhanced compaction C^* occurs. Second, to increase the stress at C^* by 50%, porosity has to be decreased, in isolation, by 0.06 (30% relative to the range 0.18–0.38) whereas average grain diameter has to be decreased, in isolation, by 0.50 mm (53% relative to the 0.2–1.15 mm). Although the influence of porosity can be regarded as higher than the influence of grain size, our study demonstrates that, over the investigated range of porosity and grain diameter, they both exert a first-order control on the mechanical compaction of natural crustal rocks, which can span over a much broader range of porosity and grain diameters. Therefore, alongside porosity, grain diameter should become a routinely measured structural parameter when dealing with the mechanical compaction of natural crustal rocks.

Overall, we believe our study demonstrates the great suitability of sintered glass beads as crustal rock analogs and the great opportunity they embody for studying microstructural parameters such as porosity and average grain diameter in isolation. Since mixtures of glass beads of different diameters can be prepared, variably polydisperse sintered samples can be synthesized and used to investigate the influence of grain size distribution and polydispersivity on mechanical and hydraulic behavior. Further, the addition of cement and/or other materials to the glass bead mixtures could also be considered in order to sharpen our understanding of the deconvolved influence of microstructural parameters on the mechanical and hydraulic properties of crustal rocks.

Data Availability Statement

The data supporting the manuscript's analysis and conclusions is available at https://doi.org/10.6084/m9.figshare.13208192.

Acknowledgments
This paper has benefitted from constructive reviews by Douglas Schmitt, Sergey Stanchits, and one anonymous reviewer. Jérôme Fortin, Mai-linh Doan, Jérémie Vasseur, and Dominique de Ligny are thanked for the discussions. The authors thank Bertrand Renaudié for the preparation of the samples and Gilles Morvan for his assistance using the SEM. The first author acknowledges funding from the Doctoral School at the University of Strasbourg. This study was partially funded by LabEx Grant ANR-11-LABX- 0050_G-EAU-THERMIE-PROFONDE (this research therefore benefited from state funding managed by the Agence National de la Recherche (ANR) as part ofthe "Investissements d'avenir" program).

References

Ablay, G., & Hürlimann, M. (2000). Evolution of the north flank of Tenerife by recurrent giant landslides. *Journal of Volcanology and Geothermal Research*, *103*(1–4), 135–159. https://doi.org/10.1016/S0377-0273(00)00220-1

Alassi, H. T. I., Li, L., & Holt, R. M. (2006). Discrete element modeling of stress and strain evolution within and outside a depleting reservoir. *Pure And Applied Geophysics*, *163*, 1131–1151. https://doi.org/10.1007/3-7643-7712-7_13

Atapour, H., & Mortazavi, A. (2018). The influence of mean grain size on unconfined compressive strength of weakly consolidated reservoir sandstones. *Journal of Petroleum Science and Engineering*, *171*, 63–70. https://doi.org/10.1016/j.petrol.2018.07.029

Atkinson, B. K., & Meredith, P. G. (1987). Experimental fracture mechanics data for rocks and minerals. In *Fracture mechanics of rock* (pp. 477–519). London:Academic Press Inc. Ltd.

Bakker, R. R., Violay, M. E. S., Benson, P. M., & Vinciguerra, S. C. (2015). Ductile flow in sub-volcanic carbonate basement as the main control for edifice stability: New experimental insights. *Earth and Planetary Science Letters*, *430*, 533–541. https://doi.org/10.1016/j.epsl.2015.08.017

Bansal, N. P., & Doremus, R. H. (2013). *Handbook of glass properties* (pp. 1–680). Orlando, FL: Elsevier. https://doi.org/10.1016/C2009-0-21785-5

Baud, P., Exner, U., Lommatzsch, M., Reuschlé, T., & Wong, T.-f. (2017). Mechanical behavior, failure mode, and transport properties in a porous carbonate. *Journal of Geophysical Research: Solid Earth*, *122*, 7363–7387. https://doi.org/10.1002/2017JB014060

Baud, P., Klein, E., & Wong, T.-f. (2004). Compaction localization in porous sandstones: Spatial evolution of damage and acoustic emission activity. *Journal of Structural Geology*, *26*(4), 603–624. https://doi.org/10.1016/j.jsg.2003.09.002

Baud, P., Reuschlé, T., Ji, Y., Cheung, C. S. N., & Wong, T. f. (2015). Mechanical compaction and strain localization in Bleurswiller sandstone. *Journal of Geophysical Research: Solid Earth*, *120*, 6501–6522. https://doi.org/10.1002/2015JB012192

Baud, P., Vajdova, V., & Wong, T. (2006). Shear-enhanced compaction and strain localization: Inelastic deformation and constitutive modeling of four porous sandstones. *Journal of Geophysical Research*, *111*, B12401. https://doi.org/10.1029/2005JB004101

Baud, P., Wong, T.-f., & Zhu, W. (2014). Effects of porosity and crack density on the compressive strength of rocks. *International Journal of Rock Mechanics and Mining Sciences*, *67*, 202–211. https://doi.org/10.1016/j.ijrmms.2013.08.031

Bedford, J. D., Faulkner, D. R., Wheeler, J., & Leclère, H. (2019). High-resolution mapping of yield curve shape and evolution for high-porosity sandstone. *Journal of Geophysical Research: Solid Earth*, *124*, 5450–5468. https://doi.org/10.1029/2018JB016719

Berge, P. A., Bonner, B. P., & Berryman, J. G. (1995). Ultrasonic velocity-porosity relationships for sandstone analogs made from fused glass beads. *Geophysics*, *60*(1), 108–119. https://doi.org/10.1190/1.1443738

Bernabé, Y., Mok, U., & Evans, B. (2003). Permeability-porosity relationships in rocks subjected to various evolution processes. *Thermo-Hydro-Mechanical Coupling in Fractured Rock*, *160*, 937–960. https://doi.org/10.1007/978-3-0348-8083-1_9

Bjørlykke, K. (2006). Effects of compaction processes on stresses, faults, and fluid flow in sedimentary basins: Examples from the Norwegian Margin. *Geological Society Special Publication*, *253*(1), 359–379. https://doi.org/10.1144/GSL.SP.2006.253.01.19

Blair, S. C., Berge, P. A., & Berryman, J. G. (1993). *Two-point correlation functions to characterize microgeometry and estimate permeabilities of synthetic and natural sandstones*. Livermore, CA: Lawrence Livermore National Laboratory (LLNL). https://doi.org/10.2172/10182383

Bloch, S., Lander, R. H., & Bonnell, L. (2002). Anomalously high porosity and permeability in deeply buried sandstone reservoirs: Origin and predictability. *The American Association of Petroleum Geologists*, *86*(2), 301–328. https://doi.org/10.1306/61EEDABC-173E-11D7-8645000102C1865D

Bourbie, T., & Zinszner, B. (1985). Hydraulic and acoustic properties as a function of porosity in Fontainebleau sandstone. *Journal of Geophysical Research*, *90*(4), 524–532. https://doi.org/10.1029/jb090ib13p11524

Bouzidi, Y., & Schmitt, D. R. (2012). Incidence-angle-dependent acoustic reflections from liquid-saturated porous solids. *Geophysical Journal International*, *191*(3), 1427–1440. https://doi.org/10.1111/j.1365-246X.2012.05695.x

Buscarnera, G., Chen, Y., Lizárraga, J., & Zhang, R. (2020). Multi-scale simulation of rock compaction through breakage models with microstructure evolution. *Proceedings of the International Association of Hydrological Sciences*, *382*, 421–425. https://doi.org/10.5194/piahs-382-421-2020

Caruso, L., Simmons, G., & Wilkens, R. (1985). The physical properties of a set of sandstones—Part I. The samples. *International Journal of Rock Mechanics and Mining Sciences & Geomechanics Abstracts*, *22*(6), 381–392. https://doi.org/10.1016/0148-9062(85)90003-8

Castagna, J. P., & Backus, M. M. (1993). *Offset-dependent reflectivity—Theory and practice of AVO analysis*. Tulsa, OK: Society of Exploration Geophysicists. https://doi.org/10.1190/1.9781560802624

Chang, C., Zoback, M. D., & Khaksar, A. (2006). Empirical relations between rock strength and physical properties in sedimentary rocks. *Journal of Petroleum Science and Engineering*, *51*(3–4), 223–237. https://doi.org/10.1016/j.petrol.2006.01.003

Chapman, S., Quintal, B., Holliger, K., Baumgartner, L., & Tisato, N. (2018). Laboratory measurements of seismic attenuation and Young's modulus dispersion in a partially and fully water-saturated porous sample made of sintered borosilicate glass. *Geophysical Prospecting*, *66*(7), 1384–1401. https://doi.org/10.1111/1365-2478.12643

Cheung, C. S. N., Baud, P., & Wong, T. (2012). Effect of grain size distribution on the development of compaction localization in porous sandstone. *Geophysical Research Letters*, *39*, L21302. https://doi.org/10.1029/2012GL053739

Concha-Dimas, A., Cerca, M., Rodríguez, S. R., & Watters, R. J. (2005). Geomorphological evidence of the influence of pre-volcanic basement structure on emplacement and deformation of volcanic edifices at the Cofre de Perote-Pico de Orizaba chain and implications for avalanche generation. *Geomorphology*, *72*(1–4), 19–39. https://doi.org/10.1016/j.geomorph.2005.05.004

Dardis, O., & Mccloskey, J. (1998). Permeability porosity relationships from numerical simulations of fluid flow. *Geophysical Research Letters*, *25*(9), 1471–1474. https://doi.org/10.1029/98GL01061

David, C., Menéndez, B., & Bernabé, Y. (1998). The mechanical behavior of synthetic sandstone with varying brittle cement content. *International Journal of Rock Mechanics and Mining Sciences*, *35*(6), 759–770. https://doi.org/10.1016/S0148-9062(98)00003-5

de Bono, J., McDowell, G., & Wanatowski, D. (2015). Investigating the micro mechanics of cemented sand using DEM. *International Journal for Numerical and Analytical Methods in Geomechanics*, *39*(6), 655–675. https://doi.org/10.1002/nag.2340

den Brok, S. W. J., David, C., & Bernabé, Y. (1997). Preparation of synthetic sandstones with variable cementation for studying the physical properties of granular rocks. *Comptes Rendus de l'Academie des Sciences—Series IIA: Earth and Planetary Science*, *325*(7), 487–492. https://doi.org/10.1016/S1251-8050(97)89866-7

Doyen, P. M. (1988). Permeability, conductivity, and pore geometry of sandstone. *Journal of Geophysical Research*, *93*(B7), 7729–7740. https://doi.org/10.1029/JB093iB07p07729

Eberhart-Phillips, D., Han, D., & Zoback, M. D. (1989). Empirical relationships among seismic velocity, effective pressure, porosity, and clay content in sandstone. *Geophysics*, *54*(1), 82–89.

Fabre, D., & Gustkiewicz, J. (1997). Poroelastic properties of limestones and sandstones under hydrostatic conditions. *International Journal of Rock Mechanics and Mining Sciences*, *34*(1), 127–134. https://doi.org/10.1016/S1365-1609(97)80038-X

Farquharson, J. I., Baud, P., & Heap, M. J. (2017). Inelastic compaction and permeability evolution in volcanic rock. *Solid Earth*, *8*(2), 561–581. https://doi.org/10.5194/se-8-561-2017

Fortin, J., Schubnel, A., & Guéguen, Y. (2005). Elastic wave velocities and permeability evolution during compaction of Bleurswiller sandstone. *International Journal of Rock Mechanics and Mining Sciences*, *42*(7–8 Spec. Iss.), 873–889. https://doi.org/10.1016/j.ijrmms.2005.05.002

Fortin, J., Stanchits, S., Dresen, G., & Guéguen, Y. (2006). Acoustic emission and velocities associated with the formation of compaction bands in sandstone. *Journal of Geophysical Research*, *111*(10), 1–16. https://doi.org/10.1029/2005JB003854

Fossen, H., Schultz, R. A., & Torabi, A. (2011). Conditions and implications for compaction band formation in the Navajo Sandstone, Utah. *Journal of Structural Geology*, *33*(10), 1477–1490. https://doi.org/10.1016/j.jsg.2011.08.001

Frenkel, J. (1945). Viscous flow of crystalline bodies under the action of surface tension. *Journal of Physics*, *9*, 385.

Gambolati, G., Ferronato, M., & Teatini, P. (2006). Reservoir compaction and land subsidence. *Revue Européenne de Génie Civil*, *10*(6–7), 731–762. https://doi.org/10.1080/17747120.2006.9692854

Ghazvinian, E., Diederichs, M. S., & Quey, R. (2014). 3D random Voronoi grain-based models for simulation of brittle rock damage and fabric-guided micro-fracturing. *Journal of Rock Mechanics and Geotechnical Engineering*, *6*(6), 506–521. https://doi.org/10.1016/j.jrmge.2014.09.001

Grunder, A., & Russell, J. K. (2005). Welding processes in volcanology: Insights from field, experimental, and modeling studies. *Journal of Volcanology and Geothermal Research*, *142*(1–2 Spec. Iss.), 1–9. https://doi.org/10.1016/j.jvolgeores.2004.10.010

Guéguen, Y., & Boutéca, M. (2004). *Mechanics of fluid saturated rocks*. Cambridge, MA: Elsevier Academic Press.

Guéguen, Y., & Fortin, J. (2013). Elastic envelopes of porous sandstones. *Geophysical Research Letters*, *40*, 3550–3555. https://doi.org/10.1002/grl.50676

Guyon, E., Oger, L., & Plona, T. J. (1987). Transport properties in sintered porous media composed of two particle sizes. *Journal of Physics D Applied Physics*, *20*(12), 1637–1644. https://doi.org/10.1088/0022-3727/20/12/015

Haeri, S. M., Hosseini, S. M., Toll, D. G., & Yasrebi, S. S. (2005). The behavior of an artificially cemented sandy gravel. *Geotechnical & Geological Engineering*, *23*(5), 537–560. https://doi.org/10.1007/s10706-004-5110-7

Hangx, S. J. T., & Brantut, N. (2019). Micromechanics of high-pressure compaction in granular quartz aggregates. *Journal of Geophysical Research: Solid Earth*, *124*, 6560–6580. https://doi.org/10.1029/2018JB016494

Harnett, C. E., Thomas, M. E., Purvance, M. D., & Neuberg, J. (2018). Using a discrete element approach to model lava dome emplacement and collapse. *Journal of Volcanology and Geothermal Research*, *359*, 68–77. https://doi.org/10.1016/j.jvolgeores.2018.06.017

Heap, M. J., Baud, P., McBeck, J. A., Renard, F., Carbillet, L., & Hall, S. A. (2020). Imaging strain localisation in porous andesite using digital volume correlation. *Journal of Volcanology and Geothermal Research*, *404*, 107038. https://doi.org/10.1016/j.jvolgeores.2020.107038

Heap, M. J., Brantut, N., Baud, P., & Meredith, P. G. (2015). Time-dependent compaction band formation in sandstone. *Journal of Geophysical Research: Solid Earth*, *120*, 4808–4830. https://doi.org/10.1002/2015JB012022

Heap, M. J., Farquharson, J. I., Baud, P., Lavallée, Y., & Reuschlé, T. (2015). Fracture and compaction of andesite in a volcanic edifice. *Bulletin of Volcanology*, *77*(6). https://doi.org/10.1007/s00445-015-0938-7

Heap, M. J., Kennedy, B. M., Pernin, N., Jacquemard, L., Baud, P., Farquharson, J. I., et al. (2015). Mechanical behavior and failure modes in the Whakaari (White Island volcano) hydrothermal system, New Zealand. *Journal of Volcanology and Geothermal Research*, *295*, 26–42. https://doi.org/10.1016/j.jvolgeores.2015.02.012

Heap, M. J., Kushnir, A. R. L., Gilg, H. A., Wadsworth, F. B., Reuschlé, T., & Baud, P. (2017). Microstructural and petrophysical properties of the Permo-Triassic sandstones (Buntsandstein) from the Soultz-sous-Forêts geothermal site (France). *Geothermal Energy*, *5*(1), 26. https://doi.org/10.1186/s40517-017-0085-9

Heap, M. J., & Wadsworth, F. B. (2016). Closing an open system: Pore pressure changes in permeable edifice rock at high strain rates. *Journal of Volcanology and Geothermal Research*, *315*, 40–50. https://doi.org/10.1016/J.JVOLGEORES.2016.02.011

Hol, S., Van Der Linden, A., Bierman, S., Marcelis, F., & Makurat, A. (2018). Rock physical controls on production-induced compaction in the Groningen field. *Scientific Reports*, *8*(1), 7156. https://doi.org/10.1038/s41598-018-25455-z

Johnson, D. L., & Plona, T. J. (1982). Acoustic slow waves and the consolidation transition. *Journal of the Acoustical Society of America*, *72*(2), 556–565. https://doi.org/10.1121/1.388036

Katsman, R., Aharonov, E., & Scher, H. (2005). Numerical simulation of compaction bands in high-porosity sedimentary rock. *Mechanics of Materials*, *37*(1), 143–162. https://doi.org/10.1016/j.mechmat.2004.01.004

Klein, E., Baud, P., Reuschlé, T., & Wong, T.-f. (2001). Mechanical behavior and failure mode of Bentheim sandstone under triaxial compression. *Physics and Chemistry of the Earth—A: Solid Earth and Geodesy*, *26*(1–2), 21–25. https://doi.org/10.1016/S1464-1895(01)00017-5

Krohn, C. E. (1988). Sandstone fractal and Euclidean pore volume distributions. *Journal of Geophysical Research*, *93*(B4), 3286–3296. https://doi.org/10.1029/JB093iB04p03286

Kuczynski, G. C. (1949). Study of the sintering of glass. *Journal of Applied Physics*, *20*(12), 1160–1163. https://doi.org/10.1063/1.1698291

Lemée, C., & Guéguen, Y. (1996). Modeling of porosity loss during compaction and cementation of sandstones. *Geology*, *24*(10), 875. https://doi.org/10.1130/0091-7613(1996)024<0875:MOPLDC>2.3.CO;2

Lindquist, W. B., Venkatarangan, A., Dunsmuir, J. R., & Wong, T. (2000). Pore and throat size distributions measured from synchrotron X-ray tomographic images of Fontainebleau sandstones. *Journal of Geophysical Research*, *105*(B9), 509–521. https://doi.org/10.1029/2000JB900208

Louis, L., Baud, P., & Rolland, A. (2009). Compaction localization in high porosity sandstones with various degrees of heterogeneity: Insight from X-ray computed tomography. In ROCKENG09: Proceedings of the 3rd CANUS rock mechanics Symposium (2009, pp. 1–2).

Louis, L., Baud, P., & Wong, T. (2007). Characterization of pore-space heterogeneity in sandstone by X-ray computed tomography. *Geological Society Special Publication*, *284*, 127–146. https://doi.org/10.1144/SP284.9

Louis, L., Wong, T.-f., Baud, P., & Tembe, S. (2006). Imaging strain localization by X-ray computed tomography: Discrete compaction bands in Diemelstadt sandstone. *Journal of Structural Geology*, *28*(5), 762–775. https://doi.org/10.1016/j.jsg.2006.02.006

Mackenzie, J. K., & Shuttleworth, R. (1949). A phenomenological theory of sintering. *Proceedings of the Physical Society Section B*, *62*(12), 833. https://doi.org/10.1088/0370-1301/62/12/310

Marketos, G., & Bolton, M. D. (2009). Compaction bands simulated in discrete element models. *Journal of Structural Geology*, *31*(5), 479–490. https://doi.org/10.1016/j.jsg.2009.03.002

Menéndez, B., Zhu, W., & Wong, T.-F. (1996). Micromechanics of brittle faulting and cataclastic flow in Berea sandstone. *Journal of Structural Geology*, *18*(1), 1–16. https://doi.org/10.1016/0191-8141(95)00076-P

Morgan, J. K., & McGovern, P. J. (2005). Discrete element simulations of gravitational volcanic deformation: 1. Deformation structures and geometries. *Journal of Geophysical Research*, *110*, B05402. https://doi.org/10.1029/2004JB003252

Nagel, N. B. (2001). Compaction and subsidence issues within the petroleum industry: From Wilmington to Ekofisk and beyond. *Physics and Chemistry of the Earth—Part A: Solid Earth and Geodesy*, *26*(1–2), 3–14. https://doi.org/10.1016/S1464-1895(01)00015-1

Nelson, P. H., & Kibler, J. E. (2003). *A catalog of porosity and permeability from Core Plugs in siliciclastic rocks*. Retrieved from https://pubs.usgs.gov/of/2003/ofr-03-420/ofr-03-420.html#References

Olsson, W. A. (1999). Theoretical and experimental investigation of compaction bands in porous rock. *Journal of Geophysical Research*, *104*(B4), 7219–7228. https://doi.org/10.1029/1998JB900120

Papadopoulos, L., Porter, M. A., Daniels, K. E., Bassett, D. S., & Estrada, E. (2018). Network analysis of particles and grains. *Journal of Complex Networks*, *6*(4), 485–565. https://doi.org/10.1093/comnet/cny005

Paterson, M. S., & Wong, T. (2005). *Experimental rock deformation: The brittle field* (2nd ed.). Berlin: Springer Verlag.

Plona, T. J. (1980). Observation of a second bulk compressional wave in a porous medium at ultrasonic frequencies. *Applied Physics Letters*, *36*(4), 259–261. https://doi.org/10.1063/1.91445

Quane, S. L., Russell, J. K., & Friedlander, E. A. (2009). Time scales of compaction in volcanic systems. *Geology*, *37*(5), 471–474. https://doi.org/10.1130/G25625A.1

Rogers, J. J. W., & Head, W. B. (1961). Relationships between porosity, median size, and sorting coefficients of synthetic sands. *Journal of Sedimentary Research*, *31*(3), 467–470. https://doi.org/10.1306/74d70ba5-2b21-11d7-8648000102c1865d

Rutter, E. H., & Glover, C. T. (2012). The deformation of porous sandstones; are Byerlee friction and the critical state line equivalent? *Journal of Structural Geology*, *44*, 129–140. https://doi.org/10.1016/j.jsg.2012.08.014

Saadi, F. A., Wolf, K.-H., & van Kruijsdijk, C. (2017). Characterization of Fontainebleau sandstone: Quartz overgrowth and its impact on pore-throat framework. *Journal of Petroleum & Environmental Biotechnology*, *8*(3), 1–12. https://doi.org/10.4172/2157-7463.1000328

Sammis, C. G., & Ashby, M. F. (1986). The failure of brittle porous solids under compressive stress states. *Acta Metallurgica*, *34*(3), 511–526. https://doi.org/10.1016/0001-6160(86)90087-8

Scherer, M. (1987). Parameters influencing porosity in sandstones: A model for sandstone porosity prediction. *American Association of Petroleum Geologists Bulletin*, *71*(5), 485–491. https://doi.org/10.1306/94886ed9-1704-11d7-8645000102c1865d

Schöpfer, M. P. J., Abe, S., Childs, C., & Walsh, J. J. (2009). The impact of porosity and crack density on the elasticity, strength and friction of cohesive granular materials: Insights from DEM modeling. *International Journal of Rock Mechanics and Mining Sciences*, *46*(2), 250–261. https://doi.org/10.1016/j.ijrmms.2008.03.009

Schultz, R. A., Okubo, C. H., & Fossen, H. (2010). Porosity and grain size controls on compaction band formation in Jurassic Navajo sandstone. *Geophysical Research Letters*, *37*, L22306. https://doi.org/10.1029/2010GL044909

Scott, T. E., & Nielsen, K. C. (1991). The effects of porosity on the brittle-ductile transition in sandstones. *Journal of Geophysical Research*, *96*(90), 405–414. https://doi.org/10.1029/90JB02069

Selley, R. C. (2004). Sedimentary rocks: Mineralogy and classification. In *Encyclopedia of geology* (pp. 25–37). Amsterdam, Netherlands: Elsevier Inc. https://doi.org/10.1016/B0-12-369396-9/00304-X

Sternlof, K. R., Rudnicki, J. W., & Pollard, D. D. (2005). Anticrack inclusion model for compaction bands in sandstone. *Journal of Geophysical Research*, *110*, B11403. https://doi.org/10.1029/2005JB003764

Sulem, J., & Ouffroukh, H. (2006). Hydromechanical behavior of Fontainebleau sandstone. *Rock Mechanics and Rock Engineering*, *39*(3), 185–213. https://doi.org/10.1007/s00603-005-0065-4

Sun, Z., Tang, H., Espinoza, D. N., Balhoff, M. T., & Killough, J. E. (2018a). Discrete element modeling of grain crushing and implications on reservoir compaction. *Journal of Petroleum Science and Engineering*, *171*, 431–439. https://doi.org/10.1016/j.petrol.2018.07.046

Sun, Z., Tang, H., Espinoza, D. N., Balhoff, M. T., & Killough, J. E. (2018b). Pore-to reservoir-scale modeling of depletion-induced compaction and implications on production rate. *Paper presented at the SPE Annual Technical Conference and Exhibition*, Dallas, Texas. https://doi.org/10.2118/191390-ms

Taylor, S. K., Nicol, A., & Walsh, J. J. (2008). Displacement loss on growth faults due to sediment compaction. *Journal of Structural Geology*, *30*(3), 394–405. https://doi.org/10.1016/j.jsg.2007.11.006

Tembe, S., Baud, P., & Wong, T. (2008). Stress conditions for the propagation of discrete compaction bands in porous sandstone. *Journal of Geophysical Research*, *113*, B09409. https://doi.org/10.1029/2007JB005439

Tembe, S., Vajdova, V., Wong, T., & Zhu, W. (2006). Initiation and propagation of strain localization in circumferentially notched samples of two porous sandstones. *Journal of Geophysical Research*, *111*, B02409. https://doi.org/10.1029/2005JB003611

Torquato, S. (2002). *Random heterogeneous materials: Microstructure and macroscopic properties*. Berlin: Springer.

Van Wyk De Vries, B., & Borgia, A. (1996). The role of basement in volcano deformation. *Geological Society, London, Special Publications*, *110*(1), 95–110. https://doi.org/10.1144/GSL.SP.1996.110.01.07

Van Wyk De Vries, B., & Francis, P. W. (1997). Catastrophic collapse at stratovolcanoes induced by gradual volcano spreading. *Nature*, *387*(6631), 387–390. https://doi.org/10.1038/387387a0

Vasseur, J., Wadsworth, F. B., Lavallée, Y., & Dingwell, D. B. (2016). Dynamic elastic moduli during isotropic densification of initially granular media. *Geophysical Journal International*, *204*(3), 1721–1728. https://doi.org/10.1093/gji/ggv550

Voight, B. (2000). Structural stability of andesite volcanoes and lava domes. *Philosophical Transactions of the Royal Society of London, Series A: Mathematical, Physical and Engineering Sciences*, *358*(1770), 1663–1703. https://doi.org/10.1098/rsta.2000.0609

Wadsworth, F. B., Vasseur, J., Llewellin, E. W., Dobson, K. J., Colombier, M., Von Aulock, F. W., et al. (2017). Topological inversions in coalescing granular media control fluid-flow regimes. *Physical Review E*, *96*(3), 33113. https://doi.org/10.1103/PhysRevE.96.033113

Wadsworth, F. B., Vasseur, J., Llewellin, E. W., Schauroth, J., Dobson, K. J., Scheu, B., & Dingwell, D. B. (2016). Sintering of viscous droplets under surface tension. *Proceedings of the Royal Society A: Mathematical, Physical and Engineering Science*, *472*(2188), 20150780. https://doi.org/10.1098/rspa.2015.0780

Wadsworth, F. B., Vasseur, J., Schauroth, J., Llewellin, E. W., Dobson, K. J., Havard, T., et al. (2019). A general model for welding of ash particles in volcanic systems validated using in situ X-ray tomography. *Earth and Planetary Science Letters*, *525*, 115726. https://doi.org/10.1016/j.epsl.2019.115726

Walsh, J. B. (1965). The effect of cracks on the compressibility of rock. *Journal of Geophysical Research*, *70*(2), 381–389. https://doi.org/10.1029/JB083iB09p04459

Wang, B. S., Chen, Y., & Wong, T. (2005). Compaction localization in porous sandstone: Acoustic emission activity, microstructural development and discrete element simulation. In *11th International Conference on Fracture 2005, ICF11* (Vol. 4, pp. 2421–2424). Red Hook, NY: Curran Associates, Inc.

Wasantha, P. L. P., Ranjith, P. G., Zhao, J., Shao, S. S., & Permata, G. (2015). Strain rate effect on the mechanical behavior of sandstones with different grain sizes. *Rock Mechanics and Rock Engineering*, *48*(5), 1883–1895. https://doi.org/10.1007/s00603-014-0688-4

Weng, M.-C., & Li, H.-H. (2012). Relationship between the deformation characteristics and microscopic properties of sandstone explored by the bonded-particle model. *International Journal of Rock Mechanics and Mining Sciences*, *56*, 34–43. https://doi.org/10.1016/J.IJRMMS.2012.07.003

Winkler, K. W. (1985). Dispersion analysis of velocity and attenuation in Berea sandstone. *Journal of Geophysical Research*, *90*(B8), 6793–6800. https://doi.org/10.1029/jb090ib08p06793

Wong, T. (1990). Mechanical compaction and the brittle-ductile transition in porous sandstones. *Geological Society Special Publication*, *54*, 111–122. https://doi.org/10.1144/GSL.SP.1990.054.01.12

Wong, T.-f., & Baud, P. (2012). The brittle-ductile transition in porous rock: A review. *Journal of Structural Geology*, *44*, 25–53. https://doi.org/10.1016/j.jsg.2012.07.010

Wong, T.-f., Baud, P., & Klein, E. (2001). Localized failure modes in a compactant porous rock. *Geophysical Research Letters*, *28*(13), 2521–2524. https://doi.org/10.1029/2001GL012960

Wong, T.-f., David, C., & Zhu, W. (1997). The transition from brittle faulting to cataclastic flow in porous sandstones: Mechanical deformation. *Journal of Geophysical Research*, *102*(B2), 3009–3025. https://doi.org/10.1029/96JB03281

Wong, T.-f., Szeto, H., & Zhang, J. (1992). Effect of loading path and porosity on the failure mode of porous rocks. *Applied Mechanics Reviews*, *45*(8), 281–293. https://doi.org/10.1115/1.3119759

Xu, T., Fu, T. F., Heap, M. J., Meredith, P. G., Mitchell, T. M., & Baud, P. (2020). Mesoscopic damage and fracturing of heterogeneous brittle rocks based on three-dimensional polycrystalline discrete element method. *Rock Mechanics and Rock Engineering*, *53*, 5389–5409. https://doi.org/10.1007/s00603-020-02223-y

Yin, H., & Dvorkin, J. (1994). Strength of cemented grains. *Geophysical Research Letters*, *21*(10), 903–906. https://doi.org/10.1029/93GL03535

Zhang, J., Wong, T.-F., & Davis, D. M. (1990). Micromechanics of pressure-induced grain crushing in porous rocks. *Journal of Geophysical Research*, *95*(B1), 341–352. https://doi.org/10.1029/JB095iB01p00341

Zhu, W., Baud, P., Vinciguerra, S., & Wong, T. (2011). Micromechanics of brittle faulting and cataclastic flow in Alban Hills tuff. *Journal of Geophysical Research*, *116*, B06209. https://doi.org/10.1029/2010JB008046

Zhu, W., Baud, P., & Wong, T. (2010). Micromechanics of cataclastic pore collapse in limestone. *Journal of Geophysical Research*, *115*, B04405. https://doi.org/10.1029/2009JB006610